Cloud Structure and Physical Conditions in Star-forming Regions from Optical Observations. II. Analysis

K. Pan[1,2], S.R. Federman[1], Y. Sheffer[1], and B-G Andersson[3]

ABSTRACT

To complement the optical absorption-line survey of diffuse molecular gas in Paper I, we obtained and analyzed far ultraviolet H_2 and CO data on lines of sight toward stars in Cep OB2 and Cep OB3. Possible correlations between column densities of different species for individual velocity components, not total columns along a line of sight as in the past, were examined and were interpreted in terms of cloud structure. The analysis reveals that there are two kinds of CH in diffuse molecular gas: CN-like CH and CH^+-like CH. Evidence is provided that CO is also associated with CN in diffuse molecular clouds. Different species are distributed according to gas density in the diffuse molecular gas. Both calcium and potassium may be depleted onto grains in high density gas, but with different dependences on local gas density. Gas densities for components where CN was detected were inferred from a chemical model. Analysis of cloud structure indicates that our data are generally consistent with the large-scale structure suggested by maps of CO millimeter-wave emission. On small scales, the gas density is seen to vary by factors greater than 5.0 over scales of $\sim 10,000$ AU. The relationships between column densities of CO and CH with that of H_2 along a line of sight show similar slopes for the gas toward Cep OB2 and OB3, but the CO/H_2 and CH/H_2 ratios tend to differ which we ascribe to variation in average density along the line of sight.

Subject headings: ISM: clouds — ISM: structure — ISM: molecules — ISM: atoms — ISM: abundances — stars: formation

[1]Department of Physics and Astronomy, University of Toledo, Toledo, OH 43606; steven.federman@utoledo.edu; ysheffer@physics.utoledo.edu.

[2]Current address: Department of Physics and Astronomy, Bowling Green State University, Bowling Green, OH 43403; kpan@hubble.bgsu.edu.

[3]Department of Physics and Astronomy, Johns Hopkins University, Baltimore, MD 21218; bg@pha.jhu.edu.

1. INTRODUCTION

The physical and chemical state in the interstellar medium (ISM) continuously changes through the combination of star formation and stellar death (Cox & Smith 1974; Jenkins & Meloy 1974; McKee 1990; Thornton et al. 1998; Marri & White 2004). The evolution of a galaxy is governed to a large extent by these processes. The final stages of star formation involve the disruption of interstellar material from which the stars formed. If enough material is available in interstellar clouds forming O and B stars, one generation of stars can lead to the formation of a second generation, and so forth, but eventually the cloud remnants can no longer sustain star formation. The propagation of star formation occurs in regions of enhanced gas density behind shocks (e.g. Elmegreen & Lada 1977; McKee & Tan 2003). Early type (O and B) stars are associated with stellar winds, expanding H II regions, and supernova explosions that lead to shocks in the surrounding medium. Since these stars tend to form in clusters (Clark et al. 2005), the effects are magnified as seen in the Magellanic Clouds. Clearly, knowledge of the physical conditions and chemical composition of the ISM in star-forming regions will help us understand the above processes and their effects on the evolution of the ISM and the Galaxy.

High-resolution optical observations of interstellar absorption (e.g., Welty & Hobbs 2001; Pan et al. 2004, hereafter Paper I) have revealed complex velocity structure on many Galactic lines of sight, especially on sight lines through star-forming clouds. Determination of the physical properties of individual interstellar clouds from observations of absorption lines requires high spectral resolution to distinguish the individual components contributing to the generally complex line profiles. Furtheremore, ultraviolet (UV) spectra provide considerable information on abundances and general physical conditions in the ISM (e.g., Spitzer & Jenkins 1975). In Paper I, we presented high-resolution optical spectra of interstellar CN, CH, CH^+, Ca I, K I, and Ca II absorption along 29 lines of sight in three star-forming regions, ρ Oph, Cep OB2, and Cep OB3. We obtained velocity component structure by simultaneously analyzing the spectra of the six species along a given sightline. Column densities and Doppler parameters of the individual velocity components were derived through profile fitting. To complement the results of the optical survey, presented in Paper I, we here present an analysis of far ultraviolet (FUV) spectra of 15 of the stars in that sample. The FUV data were either acquired in dedicated observing programs or extracted from the existing data archives of the *Far Ultraviolet Spectroscopic Explorer* (FUSE) and *Hubble Space Telescope/Space Telescope Imaging Spectrograph* (HST/STIS). The main contribution of the present paper is an analysis of the results from Paper I and those for H_2 and CO in terms of cloud structure for gas with densities of 10 to 1500 cm^{-3}. We emphasize that our data for the diffuse molecular gas associated with the three star-forming regions probe the large-scale structure of the parent molecular cloud as it disperses. We investigate whether a connection

exists between the levels of star formation and conditions in the surrounding diffuse gas.

The remainder of the paper has the following outline. The next section gives a brief background of the three star-forming regions, and § 3 describes the FUV observations and their analysis. A comparison of Doppler parameters is the focus of § 4. In § 5, we examine correlations between column densities of different species. A chemical analysis is performed in § 6 to derive gas densities for components with CH and CN. The analysis utilizes available results for C_2 from the literature. The amount of H_2 excitation and its relationship to the chemical results is described here also. This is followed by a discussion on the distribution of species within clouds, on large- and small-scale cloud structures, and a comparison of general properties for the molecular gas in the three star-forming regions. The final section presents a summary of our work.

2. Background

The divergence in the modes of star formation is perhaps best understood in terms of the physical properties of the molecular cloud and environmental effects such as nearby H II regions. ρ Oph, Cep OB2, and Cep OB3 are three regions that provide fruitful laboratories for the investigation of cloud dispersal as a result of star formation. Our data on diffuse molecular gas, whose LSR velocities are similar to those of the radio-emitting clouds, probe the later stages of dispersal. Extensive studies (e.g., Sargent 1979; de Geus, Bronfman, & Thaddeus 1990; Patel et al. 1998) on these regions outlined basic properties for the cloud complexes.

2.1. The ρ Oph Region

The region around the star ρ Oph, also called the ρ Oph Molecular Cloud, is a well-known concentration of dark nebulae and molecular clouds with a size of about 6×5 pc^2, a total molecular mass of 80 $M_\odot$ (de Geus et al. 1990), and at a distance of 140 pc. One of its prominent characteristics is the extremely active star formation in the cloud core, where stars are heavily clustered with an estimated star-forming efficiency $\geq 20\%$ (cf. Green & Young 1992; Doppmann et al. 2003; Phelps & Barsony 2004). Radio observations (Loren 1989; de Geus et al. 1990) showed that CO molecules mainly exist within a velocity range of $V_{LSR} \sim 1.5$–5.0 km s^{-1}, and that the cloud forms the boundary between the bulk of the Ophiuchus molecular gas and the Upper-Scorpius stellar groups.

The ρ Oph Molecular Cloud is part of the Ophiuchus molecular clouds, a filamentary

system of clouds with a total molecular mass of 10^4 $M_\odot$ (de Geus 1992). The Ophiuchus molecular clouds, in turn, belong to a larger cloud complex that is associated with the Scorpio-Centaurus OB association. This OB association consists of three subgroups, Lower-Centaurus Crux (LCC), Upper-Centaurus Lupus (UCL), and Upper-Scorpius (US). Blaauw (1958) showed that the three subgroups are separated in position and age, and that the youngest subgroup lies in Upper-Scorpius, which is adjacent to the ρ Oph Molecular Cloud. Based on photometric measurements, de Geus, de Zeeuw, & Lub (1989) derived ages of 11–12, 14–15, and 5–6 Myr for the three subgroups, respectively. Somewhat surprisingly, they found that the middle subgroup, UCL, is the oldest one. They argued that either the classic picture of sequential star formation (Blaauw 1964; Elmegreen & Lada 1977) is not valid for the Sco OB2 Association as a whole because the oldest subgroup is inbetween the two younger ones, or for some unknown reason, massive star formation was initiated near the middle of the original giant molecular cloud. However, Pan (2002) conjectured that LCC and UCL may actually have a similar age. More recently, Sartori, Lepine, & Dias (2003) found that the US subgroup is 4—8 Myr old and that UCL and LCC have the same age, 16-20 Myr.

2.2.   The Cepheus Bubble

A region of enhanced infrared emission associated with Cep OB2 shows the location of a giant ring-shaped cloud system, the so called Cepheus Bubble. The distance of the Bubble is somewhat uncertain. Earlier measurements indicated distances from 700 to 900 pc (Garrison & Kormendy 1976; Kun, Balazs, & Toth 1987). Recently, de Zeeuw et al. (1999) determined the distances of nearby OB associations using proper motion and parallaxes measured by Hipparcos. They obtained a distance of 615 pc for Cep OB2. As de Zeeuw et al. noticed, their distances are systematically smaller than the previous photometric determinations. If a distance of 750 pc is adopted, the ring-shaped cloud system has a diameter of about 120 pc and the total molecular mass for the system is about 10^5 $M_\odot$ (Patel et al. 1998)[4]. A dozen star-forming regions have been identified in the rim of the Bubble. Each star-forming region has a size of a few pc, similar to that of the ρ Oph region, and total molecular mass of about 10^3 $M_\odot$. Some large star-forming regions consist of several star-forming globules. For instance, IC 1396 includes at least four star-forming globules with a total mass of about 2200 $M_\odot$ and a size of 12 pc (Patel et al. 1995); Weikard et al. (1996) reached similar

---

[4]If the distance of 615 pc, as suggested by de Zeeuw et al. (1999), is adopted, the size and mass of the cloud system will be slightly smaller. Our discussion on large- and small-scale structure will not be affected by the choice of the distance.

conclusions.

Based on measurements of CO emission, Patel et al. (1998) proposed that the Bubble was created by stellar winds, and likely supernova explosions, from now deceased stars in the cluster NGC 7160 as well as the evolved stars, VV Cep and μ Cep, in the region. Patel et al. (1998) suggested that these stars were the first generation formed. The first generation stars have an age of about 13-18 Myr. After about $\sim$ 7 Myr, the expanding shell reached a size of about 30 pc and became unstable. The instability led to the formation of a second generation of stars, current numbers of Cep OB2, which are about $\sim$ 7 Myr old. The IRAS point sources in the globules and molecular clouds associated with the Bubble are the third generation, whose formation was triggered by stellar winds from Cep OB2 stars. From H I 21 cm data, Abraham, Balazs & Kun (2000) obtained a similar picture for the formation of the Bubble. The latter model showed that a supernova explosion might have occurred as recently as about 2 Myr ago. The explosion expanded the pre-existing Bubble further.

2.3.   Cloud System Associated with Cep OB3

The molecular clouds producing the Cep OB3 Association represent a filamentary system, showing clumpy and irregular structure (Sargent 1977, 1979). The cloud system is located at a distance of about 700–800 pc (Garrison 1970; Moreno-Corral et al. 1993), with a size of $\sim$ 60×20 pc^2 and a total molecular mass of $\sim$ 10^4 $M_\odot$ (Sargent 1979). A few identified star-forming regions are embedded in the cloud system. The star-forming regions in this cloud system have a size similar to those in the Cepheus Bubble (a few pc), but have smaller total molecular mass (100–500 $M_\odot$). Our lines of sight toward Cep OB3 probe two star-forming regions in the cloud system, Cepheus B and Cepheus F, with total molecular mass of 100 and 300, respectively (Yu et al. 1996).

The Cep OB3 Association consists of two subgroups separated by $\sim$ 13 pc on the plane of the sky. Based on photometric measurements, Blaauw (1964) assigned ages of 8 and 4 Myr to the two subgroups. However, ages derived from such isochrone fitting must be treated with caution in young OB associations because masses and ages remain model dependent. Consequently, the shape of both the evolutionary tracks and of the isochrones change from one model to another, leading to discrepancies in the age estimates. Much lower ages for the younger subgroup can be found in the literature. For instance, Garmany (1973) and Assousa, Herbst & Turner (1977) obtained an age of $\sim$ 1 Myr for it. Sargent (1979) suggested that the formation of the younger group was triggered by the interaction between stellar winds of the older subgroup and the original molecular cloud.

3. FUV Observations and Analysis

In Paper I, we presented observational data for interstellar CN, CH, CH$^+$, Ca I, K I, and Ca II absorption on 29 directions in ρ Oph, Cep OB2, and Cep OB3. To complement these results, we obtained and analyzed FUV data for H$_2$ and CO. Eight stars from the sample in Paper I were observed with *FUSE* under our programs A051 and B030. For each star, reduction and calibration were performed using CALFUSE V2.4. We then re-binned the data by a factor of 4, yielding a two-pixel resolution element of ~ 0.06 Å. *FUSE* archival data for two more stars, HD 206773 and HD 217312, were downloaded from programs B071 and P193, respectively. Four additional stars have been studied before; we used their published H$_2$ column density, $N(\mathrm{H}_2)$, and $T_{1,0}$ results from Rachford et al. (2003) (under *FUSE* program P116). Although no published H$_2$ results are available for HD 208266, we included this star in our analysis because there were CH and CO observations. Moreover, these data can be utilized in tandem to predict $N(\mathrm{H}_2)$ toward HD 208266. Table 1 lists all FUV datasets that we utilized, specifying which space telescope was the source, what S/N was obtained, and which molecules were analyzed.

Three $B - X$ bands of H$_2$ (2$-$0, 3$-$0, and 4$-$0, between 1042 and 1083 Å) were chosen to model the molecule's column density. This range is covered by the four overlapping *FUSE* detector segments, LiF-1A, LiF-2B, SiC-1A, and SiC-2B, although 2$-$0 is not covered by LiF-2B. Each segment was fitted independently with the code ISMOD, which uses the simplex method to minimize the rms of the residuals down to about 10^{-4} in relative parameter steps. The fit was based on the CH cloud components in Paper I, preserving the velocity separations and relative fractions in column density among components as fixed input. We, however, allowed the b-values to vary during the fits, constraining them by the mass ratio of CH to H$_2$ and by the kinetic temperature (T) in the gas as given by the (fitted) $T_{1,0}$ rotational temperature of H$_2$ (see § 6.2). Both the thermal and non-thermal components of the velocity field were thus determined. Free parameters included the total column density, $N(\mathrm{H}_2)$, radial velocity of H$_2$, six rotational temperatures relative to the ground state, $T_{J'',0}$, and the placement of the stellar continuum. Our final H$_2$ model and the associated uncertainties were computed by averaging the results from fits of the four independent segments. In a few cases of high-J levels, where one of the four segment yielded a deviant result, that value was not included in the final average. The values of total $N(\mathrm{H}_2)$ are very robust and practically independent of the cloud structure because of the damping wings for the $J'' = 0$ and 1 lines.

For determinations of CO column density, we first searched the *HST*/STIS archive and downloaded high-resolution observations of $A - X$ bands of CO. Six stars happen to have E140H data with R $\gtrsim$ 100,000, covering $A - X$ bands blueward of ~ 1360 Å (transitions 7$-$0 and higher). For the ISMOD fits, we used f-values from Chan, Cooper & Brion (1993), see

also Morton and Noreau (1994). These values are within a few percent of those recommended by Eidelsberg et al. (1999), except for the f-value for $11-0$ where Chan et al.'s value is 11% smaller. The higher HST/STIS resolution allowed us to derive relative cloud strengths as well. When the CO along a line of sight is relatively weak, not enough fitting leverage is available from the $A - X$ bands alone. In such cases we expanded the analysis to include simultaneous fits of Rydberg bands from the $FUSE$ data with R $\approx$ 17,500. For CO toward HD 203374A, our simultaneous fits of $A - X$ and Rydberg bands were published in Sheffer, Federman, & Andersson (2003). An additional three stars have medium-resolution data from the E140M grating (R = 46,000). Despite the lower resolution, robust fits are reliably obtainable in these cases because the spectral coverage includes 14 $A - X$ bands down to the lowest S/N region around Ly-α. Nevertheless, in our fits we employed at most six bands for simultaneous solutions, making sure to include bands spanning the largest possible range in f-value. Adding more bands to the fit did not change the results significantly. Finally, for the six stars without any archival HST/STIS data, our CO modeling was based solely on the three Rydberg bands, $B - X$ $0-0$, $C - X$ $0-0$, and $E - X$ $0-0$. Understandably, the inferred CO component structure for these stars are less reliable than for those from $A - X$ bands, due to the lower resolution of $FUSE$ and the limited range in f-values sampled, which were based on the results of Federman et al. (2001). However, since the $B - X$ $0-0$ band is relatively optically thin, the total N(CO) is approximately independent of the cloud structure. The derived total H_2 and CO column densities along the fifteen lines of sight are listed in Table 2, along with the kinetic temperature ($T_{1,0}$) of H_2. For comparison, we also tabulate CH column densities from Paper I and abundance ratios (CH/H_2 and CO/H_2) along these sight lines. Table 3 provides the column densities for individual H_2 rotational levels.

4. Doppler Parameter and CN Excitation Temperature

The Doppler parameters, b-values, of individual absorption components seen for any individual species provide upper limits on the temperature and internal turbulent velocity (v_t) in the interstellar gas because $b = (2kT/m + v_t^2)^{1/2}$. If two species with significantly different atomic weight m coexist in the same volume of gas, comparison of their b-values provides estimates of the relative contributions of thermal and turbulent broadening, if both lines are fully resolved. Alternately, known temperatures and turbulent velocities for two species can allow estimates of their relative volumetric distributions. The extracted b-values in the present paper, except for CN b-values from the doublet ratio method in this section, are based on Gaussian instrumental widths.

Earlier studies suggested that CN resides in denser regions whereas CH$^+$ is found mainly

in regions of lower density (Cardelli et al. 1990; Federman et al. 1994). The CH molecule, on the other hand, can be present in both low- and high-density gas (100 vs. 600 cm^{-3}). It can be synthesized through the non-equilibrium CH$^+$ chemistry in low density diffuse clouds (Draine & Katz 1986; Zsargó & Federman 2003), and in moderately dense gas it is produced via C$^+$ + H$_2$ → CH$_2^+$ + $h\nu$ (Federman et al. 1994). However, it is not a trivial task to disentangle the amount of CH formed with CH$^+$ or associated with CN. Examining CH$^+$–like CH and CN–like CH components may elucidate the chemical schemes occurring in the gas (Lambert, Sheffer, & Crane 1990). Of our 125 CH components, there were 12 CN–like CH components, which are CH components with corresponding CN, but no CH$^+$ [N(CH$^+$) < 3.0×10^{11} cm^{-2}], at the same V_{LSR}, and 78 CH$^+$–like CH components, CH components with detected CH$^+$ at the same V$_{LSR}$ but no CN [N(CN) < 2.0×10^{11} cm^{-2}]. Typically, CH$^+$ and CN column densities are 7 times greater than these limits. Table 4 presents average b-values of the CH$^+$-like CH and the CN-like CH components, along with mean Doppler parameters of all defined components for other species. The analysis reveals that CN-like CH components have an average b-value indistinguishable from that of CN components (0.83 ± 0.11 km s^{-1} vs. 0.90 ± 0.11 km s^{-1}), whereas CH$^+$-like CH components possess a larger average b-value (1.10 ± 0.16 km s^{-1}). Simple statistical tests show that the average b-values for a given species agree within their mutual uncertainties in the diffuse gas surrounding different star-forming regions, although Cep OB3 seems to have consistently larger b-values than ρ Oph and Cep OB2. Since thermal broadening plays a minor role, our results indicate that cloud turbulence in the three regions does not differ significantly.

Compared with earlier studies, our average b-values of atomic species (Table 4) are slightly greater than those obtained from very high-resolution spectra of interstellar atomic lines. Based on spectra with resolution of 0.3-0.6 km s^{-1}, Welty and colleagues obtained median b-values of 0.66 km s^{-1} for Ca I components (Welty, Hobbs, & Morton 2003), 0.67 km s^{-1} for K I (Welty & Hobbs 2001), and 1.33 km s^{-1} for Ca II components (Welty, Morton, & Hobbs 1996). Three causes may lead to the differences. Their spectra had much higher resolution than ours so that they could discern more closely blended components which we did not, different lines of sight were probed, and the median values are slightly smaller than corresponding average values. (For example, the median b is 0.66 km s^{-1} while the corresponding average is 0.70 km s^{-1} for well defined Ca I components.) With a resolution of ∼ 0.50 km s^{-1}, Andersson, Wannier, & Crawford (2002) obtained spectra of interstellar CH absorption toward 18 stars in southern molecular cloud envelopes. Based on F-tests (Lupton 1993), they fitted all but one of these CH profiles with a single-velocity component. (However, they noticed that additional velocity components may be present). Their b-values range from 0.3 to 3.6 km s^{-1}, with an average of 1.7 km s^{-1}. This mean b-value is greater than ours, 1.04 km s^{-1} (Table 4). Because we simultaneously analyzed the spectra of six

species along a given sightline (Paper I), in general, we found more CH velocity components per line of sight. This is one of the reasons, if not main one, that our average b value is smaller than theirs. Based on ultra-high-resolution (δv $\sim$ 0.35 km s^{-1}) observations along five lines of sight, Crawford (1995) found average b-values of 0.63, 1.5, 2.3, and 0.8 km s^{-1} for CN, CH, CH$^+$, and K I components. Overall, our average Doppler parameters are in agreement with those determined by previous studies using spectra with higher resolution.

The b-value of a CN component can also be derived by using the doublet ratio (Strömgren 1948) — see also Gredel, van Dishoeck, & Black (1991). Because CN $R(1)$ and $P(1)$ absorption lines arise from the same rotational level, N''=1, the same column density should be inferred from them. Therefore, the b-value of a CN component can be determined by performing a curve of growth analysis on the $R(1)$ and $P(1)$ values of W_λ and requiring they give the same column density and b-value. To check b-values of CN components derived from the profile fitting in Paper I, we applied the doublet ratio method to eleven components where both CN $R(1)$ and $P(1)$ lines were detected and obtained an average b-value of 0.70 $\pm$ 0.14 km s^{-1}, which is closer to that of Crawford (1995) based on ultra-high-resolution spectra. Considering the uncertainties, it also agrees with the mean Doppler parameter in Table 4, which we determined from profile fitting.

Once the b-value of a CN component is determined, column densities of rotational levels of N''=0 [from CN $R(0)$] and N''=1 [from CN $R(1)$ and $P(1)$] can be derived by using a curve of growth. Knowing columns of these rotational levels allows us to obtain the CN excitation temperature, T_{ex}, of CN components. T_{ex} is governed by the Boltzmann equation,

$$T_{ex} = \frac{h\nu}{k_B} \left(ln \left[\frac{g_1 N(0)}{g_0 N(1)} \right] \right)^{-1} = \frac{5.442}{ln\,[3N(0)/N(1)]}, \tag{1}$$

where $h\nu$ is the energy separation between rotational levels N''=0 and N''=1, while g and N are the statistical weight and column density for each level. The derived CN excitation temperatures for these eleven components range from 2.55 K to 2.89 K with an average of 2.75 $\pm$ 0.10 K. The derived excitation temperatures indicate that no significant excitation in addition to that due to the CMB is observed in these cloudlets, including three components toward HD 204827 where very strong CN absorption is detected and T_{ex} is between 2.72 and 2.78 K.

The b-values in Table 4 for CO toward Cep OB2 and OB3 are most like those for CN, suggesting that these species coexist in the diffuse molecular gas probed by optical absorption. There is also a hint that the b-values for Cep OB3 are larger, as seen in other species, but in the case of CO, the difference could be the result of coarser resolution in $FUSE$ spectra for the stars in Cep OB3. Other evidence makes the connection between CO and CN

stronger. First, while the input for the synthesis of CO bands was based on the component structure seen in CH, the best fit revealed a component structure very similar to that for CN. This is illustrated in Table 5, where the *rms* deviations between CO and CH relative column density fractions on the one hand and between CO and CN on the other are presented for syntheses based on STIS spectra. Along each line of sight, the *rms* deviations are smaller for CN than for CH. The correspondence is not perfect, however, because CO and CH are detected in cases where only upper limits for CN are available (e.g., Crenny & Federman 2004). Second, there is an approximate linear relationship between $N(CO)$ and $N(CN)$ for individual velocity components. Since upper limits exist for both quantities, correlations were sought through the use of the package ASURV, revision 1.1 (see Isobe, Feigelson, & Nelson 1986; Isobe & Feigelson 1990; La Valley, Isobe, & Feigelson 1992). Using Schmitt's Method, we obtain $\log[N(CO)] = (1.16 \pm 0.13) \log[N(CN)] + (0.75 \pm 1.59)$. This analysis suggests that all but 3 of 24 limits are consistent with detections. When all data are treated as detections, Schmitt's Method gives a slope of 1.35 ± 0.17 and an intercept of $-(1.56 \pm 2.02)$ and a linear least-squares fit indicates respective values of 1.63 ± 0.16 and $-(4.89 \pm 1.85)$. The slopes are steeper when all data are considered detections because the upper limits on CN are less confining. Each of these observational effects show that columns of CO and CN are tightly coupled in the denser portions of diffuse molecular clouds, a conclusion consistent with our earlier findings (Zsargó & Federman 2003; Crenny & Federman 2004).

5. Correlations among Column Densities

Comparisons of column densities for different species provide constraints on chemical models, elemental depletions, species distributions, and the processes contributing to the ionization in diffuse clouds (e.g., Hobbs 1976; Chaffee & White 1982; Federman et al. 1994; Welty & Hobbs 2001). Based on high resolution and high S/N spectra, Paper I derived column densities for CN, CH, CH^+, Ca I, K I, and Ca II for individual velocity components along 29 lines of sight. The data set has good internal self-consistency and is also large enough to allow us to discuss correlations based on individual components rather than total line of sight columns as usually done in previous studies (e.g., Danks, Federman, & Lambert 1984; Welty et al. 2003). Therefore, presumably, this data set will provide a good view of relationships among species. We examine some possible correlations between column densities of observed species. In each case, we first perform a least-squares fit to $\log[N(Y)]$ versus $\log[N(X)]$ to obtain the linear correlation coefficient, r, and the corresponding probability of no correlation, p, — i.e., the probability for a random distribution of N measurements to result in a correlation coefficient $r' \geq r$, according to Bevington & Robinson (1992). Then,

a regression analysis[5] is performed to get the slope, intercept, and an estimate of the scatter (the root mean square distance of points from the fit line). In all the fits, we made one 3σ pass through the data to eliminate outliers. It turns out that three points are excluded from the fit for the relationship of $\log[N(CN)]$ versus $\log[N(CH^+\text{-corrected CH})]$ and one from fits of CN vs. CH, Ca I vs. K I, and Ca I vs. Ca II. Table 6 provides a summary of the correlations. The analysis shows that all correlations listed in the table have confidence levels, $1 - p$, exceeding 99.95%. In the following subsections, we describe some of these relationships.

5.1.   CH versus CH$^+$

When all CH velocity components are considered, the data set suggests a weak, at most, trend of increasing CH abundance with increasing CH$^+$ column. However, the correlation becomes much stronger when we include only CH$^+$-like CH components, as shown in the bottom panel of Figure 1. A closer look reveals that the correction is weak for components with higher CH$^+$ columns. If only components with $\log[N(CH^+)] > 12.6$ are considered, column densities of the two species are not well correlated. This is clearly indicated by the greater amount of dispersion seen at higher column densities for a linear fit to all the data. Therefore, the correlation is sought for components with $\log[N(CH^+)] \leq 12.6$.

In previous studies, based on total column densities along lines of sight, CH column densities were sometimes found well correlated with $N(CH^+)$. For instance, Crane, Lambert, & Sheffer (1995) found that lines of sight with detectable amounts of both CH and CH$^+$ show a large range in CH to CH$^+$ column density ratios, whereas Federman, Welty, & Cardelli (1998) showed that, for lines of sight with no CN detections, CH was well correlated with CH$^+$, and that the CH predicted by CH$^+$ synthesis agreed well with observations. Our findings explain why different correlations were seen in these studies. Because many of the sight lines in the study of Crane et al. have large amounts of CN, some CH on these sight lines is associated with CN instead of CH$^+$. Therefore, $N(CH)$ should not be well correlated with $N(CH^+)$. On the other hand, Federman et al. (1998) focused on lines of sight with detected CH and CH$^+$ but no corresponding CN. All CH in this study was CH$^+$-like CH and a good correlation is expected.

---

[5]We used the subroutine regrwt.f, obtained from the Penn State statistical software archive at http://www.astro.psu.edu/statcodes, with slight modifications, to perform the regressions.

5.2. CN Versus CH

The top panel of Figure 1 reveals that column densities of CN components are correlated with columns of their corresponding CH components (one component of HD 217312 was eliminated by a 3σ pass). This component-based correlation is much tighter than the sight-line-based relationship (cf. Figure 7 of Federman et al. 1994). Moreover, the correlation is even stronger when only CN-like CH components are included, as shown in the bottom panel of Figure 2. This study strengthens our previous statement, based on b-values, that CN-like CH components are closely associated with the CN components.

We have discussed CN-like CH and CH^+-like CH. How about CH components that have both corresponding CN and CH^+ components? Is a part of their CH associated with CN, and another part with CH^+? To seek answers to these questions, we calculated the amount of CH corresponding to CH^+ for these components by applying the $N(CH^+$-like CH) vs. $N(CH)$ relation given in Table 6, and subtracted the result from the total CH column density, yeilding $N(CH^+$-corrected CH). [If $\log[N(CH^+)] > 12.6$, $N(CH) = 4.0 \times 10^{12}$ cm^{-2} is taken from the total CH column as CH^+-like CH]. The top panel of Figure 2 presents the correlation between $N(CN)$ and $N(CH^+$-corrected CH), where three components are excluded from the final fitting by the 3σ pass. All three components have small amounts of CN, $(0.4—0.7) \times 10^{12}$ cm^{-2}, but are still too much for their corresponding CH^+-corrected CH in the relationship. It is possible that their amounts of CN are overestimated because columns of about 0.4×10^{12} cm^{-2} represent marginal detections. As one can see from Figure 1, the $N(CH^+$-like CH) vs. $N(CH^+)$ relationship shows quite a bit of scatter. This scatter may cause the three components to be outliers as well.

Use of CH^+-corrected CH interestingly does improve the correlation compared to the original $N(CN)$ vs. $N(CH)$ plot. The correlation coefficient slightly increases from 0.80 to 0.86. As one can see from Figure 2 and Table 6, the regression is now very similar to that for $N(CN)$ vs. $N(CN$-like CH). This analysis indicates that our assumption is a reasonable one. In other words, we conclude that there are two kinds of CH in diffuse molecular clouds: CN-like CH and CH^+-like CH. Disentangling the amount of CH in each appears possible when utilizing the relation between columns of CH^+-like CH and CH^+. In the past, only ultra-high resolution observations toward ζ Oph (Lambert et al. 1990; Crawford 1997) distinguished between these two possibilities.

5.3. K I Versus CH

Welty & Hobbs (2001) found an essentially linear relationship between N(K I) and N(CH) by using total column densities along lines of sight. Based on column densities for individual velocity components, we obtain a very similar correlation, with a slope of 0.96 $\pm$ 0.04, as shown in the upper panel of Figure 3. Three facts suggest that these two species respond very similarly to changes in physical conditions in diffuse molecular clouds: 1) the strong linear correlation between N(K I) and N(CH), 2) the similar average b-values (Table 4) and 3) the similar column density relationship for components and for lines of sight. This also implies that they generally coexist, at least in the density range sampled by these data. However, we also note that there are exceptions. A few K I components with reasonable strengths do not have corresponding CH components. For instance, the velocity component at $V_{LSR} \sim -4.3$ km s^{-1} toward HD 216532 has a K I column density of 3.2×10^{11} cm^{-2}, but no detected CH. However, there are relatively strong Ca I and Ca II lines with column densities of 5.2×10^9 cm^{-2} and 10.0×10^{11} cm^{-2}, respectively. Considering the b-value of the K I component, 1.5 km s^{-1}, is greater than the average value of 0.92 km s^{-1} (as is the case for the Ca I and Ca II component), we think this K I component may arise from a slightly lower density region where no significant amount of CH is present, but one with a relatively large volume so that a reasonably strong K I line is observed. In other words, this may indicate that K I could be distributed in less dense regions where no observable amount of CH resides.

5.4. Ca I Versus K I

The lower panel of Figure 3 presents the relationship between N(Ca I) and N(K I). The figure shows that the column densities of the two species are well correlated. However, the best fit slope of 0.60 $\pm$ 0.04, indicated by the solid line in the plot, is significantly smaller than 1.0. Compared with the relationship of Welty et al. (2003), which was based on total column densities, our best fit slope is the same as theirs (0.60 $\pm$ 0.08) while the scatter and the intercept (2.88 $\pm$ 0.47 versus 3.11 $\pm$ 0.68) are slightly smaller. Welty et al. (2003) discussed possibilities that could lead to a slope less than unity for the comparison between $\log[N$(Ca I)$]$ and $\log[N$(K I)$]$. They concluded that it is most likely that calcium depletion has a steeper dependence on local density than does potassium depletion. This is not all that unexpected because calcium is a refractory element while potassium is more volatile, having lower condensation temperature. Once again, three facts, the good correspondence in column density, similar average b-values (see Table 4), and the similar correlations between relationships based on individual components and on lines of sight, suggest that these two

species generally share comparable volumes.

In addition to above the correlations, Table 6 also lists relationships for $\log[N(\text{Ca I})]$ vs. $\log[N(\text{Ca II})]$ and $\log[N(\text{K I})]$ vs. $\log[N(\text{Ca II})]$. Column densities of these species are correlated although not as tightly as the relationships above, with about twice the scatter. The column density ratios can differ by a factor of 10 for individual components. Such a large range in column density ratios may indicate that these species do not track each other well. In other words, they seem to be probing different portions of a cloud. There are actually many Ca II components without corresponding Ca I or K I. This latter fact arises because Ca II is believed to be distributed more broadly (Welty et al. 2003).

6. Chemical Analysis

6.1. CN Chemistry

The route to CN in diffuse molecular clouds involves CH to C_2 to CN (Federman et al. 1984, 1994). We use the steady-state analytical expressions in Federman et al. (1994), with updated rate coefficients (Knauth et al. 2001; Pan, Federman, & Welty 2001), to extract estimates for gas density in the material containing CN by matching the observed column densities for CN and C_2 (when available). Steady state is appropriate for this scheme because the photochemical time scales are less than 100 yrs., much shorter than the sound-crossing time. *Observed* CH column densities are adopted for use in estimating the CN and C_2 column densities. In our earlier papers (i.e., Federman et al. 1984, 1994) the analysis is based on line-of-sight column densities, but here we obtain results for individual velocity components where CN is detected. The CH and CN column densities mainly come from the results presented in Paper I. The exception is CH toward λ Cep; we adopt the results from the ultra-high resolution measurements of Crane et al. (1995). (In passing, we note that the 2 CH components have a separation consistent with what we found for CN. Of the 2 CH^+ components, only the bluer one is associated with gas containing CN; the redder component is seen in K I absorption but not in absorption from other molecules – see Paper I.) Along several sight lines, results for C_2 are also available (Danks & Lambert 1983; Federman & Lambert 1988; Federman et al. 1994). When more than one CN component is present for a given direction, the relative amounts of C_2 in each component is taken to be the same as CN because these molecules likely coexist (Federman et al. 1994).

To extract estimates of gas densities from the chemical model (Federman et al. 1994, Pan et al. 2001), in addition to column densities of CN and CH (C_2 column provides a further constraint), O, C^+, and N abundances, temperature, and UV radiation field are needed. Our

sample contains some of the most molecular-rich diffuse clouds studied to date. Special care is necessary when choosing the appropriate atomic abundances in these circumstances. The O and C^+ abundances are now available along sight lines in our sample. Cartledge et al. (2001) found that the O abundance toward ρ Oph D and HD 207198 differs by about 1-σ from the diffuse cloud average, while that for C^+ is comparable to the average (Sofia et al. 2004). André et al. (2003) and Cartledge et al. (2004), respectively, provided results on O toward HD 206773 and λ Cep that are not atypical. Thus, we continue to use the average abundance for diffuse clouds in the chemical analysis. For C^+ this is not unreasonable because the largest CO columns encountered in our survey are about 10^{16} cm^{-2}, which represents less than 10% of the carbon budget, and the neutral carbon column densities (Jenkins & Tripp 2001) are smaller still. Most calculations are based on the average interstellar radiation field of Draine (1978) and on $T = 50$ K, the temperature commonly inferred from excitation of low-lying rotational levels in H_2 and C_2 (e.g., van Dishoeck & Black 1986; Federman et al. 1994). The latter value is not critical because the results for n are not very sensitive to T — the estimated gas densities change by less than 10% when the temperature is changed by a factor of 2 (Pan et al. 2001). For especially molecular-rich clouds, lower values for T are adopted, while slightly larger temperatures (65 K) are used for sight lines toward Cep OB3 where fewer CN components are present. These adopted temperatures and the UV radiation field are justified in §6.2.

The chemical model also involves the optical depths of grains at 1000 Å, τ_{uv}, and threshold grain optical depths for ultraviolet photons, τ_{uv}^{o}, in somewhat indirect ways. These optical depths were used to determine the amount that photodissociation rates are attenuated and a coarse treatment of the C^+ to CO transition, respectively. For most sight lines, we previously adopted $\tau_{uv} = 2A_V$ (e.g., Federman et al. 1994), but such a value does not appear to be appropriate for our sample of sight lines. As noted by Federman et al. (1994), larger grains are present toward the stars comprising ρ Oph, and a value of $1.4A_V$ is used. Though the extinction law for directions in Cep OB3 is similar to the law representing the average for diffuse sight lines, the molecular gas is more clumpy (Sargent 1979) and Federman et al. (1994) adopted $1.4A_V$ here as well. We do the same in light of the numerous components seen in K I absorption. For Cep OB2, extinction laws for several stars are available (Massa, Savage, & Fitzpatrick 1983; Savage et al. 1985; Aiello et al. 1988; Fitzpartick & Massa 1990; Megier et al. 1997), although sometimes only in tabular form. For the most part, the laws do not differ much from the average law, except for the sight line very rich in molecules — HD 204827, where the ultraviolet extinction rises quite rapidly at the shortest wavelengths (Fitzpatrick & Massa 1990). Our starting point for the directions in Cep OB2 for τ_{uv} was $2A_V$. The number of components toward stars in this association as well as in Cep OB3 created a further complication, which is compounded by the fact that foreground material along

the $\approx$ 750-pc pathlengths is likely. First, we assumed that all the molecular gas is located in the star-forming regions. Extinction only from the molecular components was considered in the chemical analysis; it was estimated from the fraction of K I column associated with CH components. The fraction always exceeded 0.50 and was usually 0.80 or more. Second, the line-of-sight extinction was used because shadowing of one diffuse molecular cloud on another is more than likely. Since photodissociation is the dominant destruction pathway for most of the clouds in our study, uncertainties in τ_{uv} lead to uncertainties of about 30% in the inferred gas densities. Since the directions under study have a significant amount of reddening [$E(B-V) \geq 0.3$ mag], but diffuse cloud abundances for C$^+$, the perscription of Federman & Huntress (1989) for treating the C$^+$ to CO transition had to be revisited. The cause of the apparent inconsistency between reddening and C$^+$ abundance is the presence of numerous molecular components along each direction in Cep OB2 and OB3. For these associations, the threshold grain optical depth for ultraviolet photons, τ_{uv}^o, was increased to 3.75 from 2.0. As a result, only toward HD 204827, where N(CN) reaches the highest values, is there likely to be much conversion of C$^+$ into CO.

The results of our analysis, which are based on the rate equations from Federman et al. (1994) with updated rate data from Knauth et al. (2001) and Pan et al. (2001), appear in Table 7. The simplified model cloud has constant density and temperature. For each cloud along a specific direction, we list the factor giving the enhancement over Draine's (1978) interstellar UV radiation field (I_{uv}), τ_{uv}, the kinetic temperature (T), the gas density [$n = n(\text{H}) + 2n(\text{H}_2)$], the observed column densities for CH, C$_2$, and CN [$N_o(\text{CH})$, $N_o(\text{C}_2)$, and $N_o(\text{CN})$], and the predicted columns for C$_2$ and CN that best match the observations [$N_p(\text{C}_2)$ and $N_p(\text{CN})$]. The column densities are given in units of 10^{12} cm^{-2}. The predicted column densities are always within 30% of the observed values; thereby providing another measure of the uncertainty in inferred gas density.

The inferred gas densities range from about 100 to slightly higher than 1000 cm^{-3}, not untypical for diffuse molecular gas, and consistent with those by Weikard et al. (1996) — based on CO observations, they estimated densities for CO cloudlets of about 500 to 2000 cm^{-3}. Our inferred densities probably represent lower limits to the true densities. First, we assumed that all the CH in a component participated in the production of CN although we find CN-like and CH$^+$-like CH (see Section 5.2). Use of the relationship between CH$^+$-like CH and CH$^+$ to account for CH in the lower density gas along the line of sight and not involved in CN chemistry is possible. We chose not to pursue this because the dispersion in the relationship (Fig. 1) could lead to unphysical results (negative columns) in some of our sample. Instead, we note that the clouds with the lowest densities are the ones most likely affected by this assumption. Second, we obtained the extinction for the molecular gas along the line of sight from the fraction of K I in CH components. The extinction would

be smaller if only the CN components were used, resulting in higher densities to offset more photodissociation.

We analyzed the CN chemistry for several of these sight lines in the past (Federman & Lambert 1988; Federman et al. 1994; Pan et al. 2001). For the most part, the inferred gas densities are similar, usually within 30%. Much of the difference is likely caused by our current emphasis on individual components along a line of sight. The other factor, highlighted by the comparison with the results of Pan et al. (2001) based on the same chemical rates, is the use of updated column densities. For example, the difference in density for the -0.8 km s^{-1} component toward HD 206267C arises from the decrease in N(CN) from 0.9×10^{12} to 0.4×10^{12} cm^{-2}.

Two sight lines, HD 207198 and HD 204827, yield surprisingly low gas densities for the large CN columns present. For HD 207198, the three CN components contain substantial amounts of CH^{+}. If the CH associated with CH^{+} does not take part in CN production and therefore must be removed from the CH column used in the chemical model, then densities a factor of 2 larger would be inferred. This modification is less effective for the clouds toward HD 204827. Instead, the low values inferred for n result from the significant extinction. The large extinction, consistent with HD 204827 lying deepest within the CO contours of any sight line in our sample (see Fig. 8), greatly lessens the importance of destruction through photodissociation. This contrasts with the results for HD 62542 where high densities are required to reproduce the large CN column on a sight line with A_V of 1 mag (Cardelli et al. 1990; Federman et al. 1994). These points are illustrated in Table 7 for the $+1.9$ km s^{-1} component toward HD 207538. The second entry shows that n increases five-fold for $I_{uv} = 5$, highlighting the importance of photochemistry for most of our sample. The third entry indicates that when about half the CH is associated with CN, n increases a factor of ~ 2.

6.2. H$_2$ Excitation

Column densities for H$_2$ rotational levels in the ground vibrational level carry information on physical conditions that provides a justification for our inputs in the chemical analysis. The relative populations of $J = 0$ and 1 give a reliable estimate for kinetic temperature (Savage et al. 1977). Since rotational transitions between ortho-H$_2$ (odd J) and para-H$_2$ (even J) are strictly forbidden, collisions involving protons and H$_2$ produce a thermal distribution between $J = 0$ and 1. High-J levels may be populated by photon pumping, collisions in shock-heated gas, and in the formation of H$_2$ molecules on dust grains. Column density ratios such as $N(4)$ and $N(2)$ yield upper limits to the UV flux causing the photon pumping when the other processes are neglected (but see Gry et al. 2005).

In Table 2, we listed kinetic temperatures from the H_2 analysis (§ 3) for lines of sight toward Cep OB2 and Cep OB3. The listed values of $T_{1,0}$ suggest that directions toward Cep OB3 have slightly higher kinetic temperatures (80 K on average) than those toward Cep OB2 (74 K). The temperatures used in the chemical analysis (§ 6.1) are somewhat lower, 65 K for Cep OB3 and 50 K for others, as would be expected for the less extensive, denser portions of a cloud where CN is detected. As for higher J levels, the observed ratios, $\log[N(4)/N(2)]$, presented in Table 3 lie between -2.68 and -0.95. Placing our results for H_2 on Fig. 3 of Browning, Tumlinson, & Shull (2003), which is based on $I_{uv} \approx 15$, allows us to infer the relevant UV flux to adopt. The data for HD 203374A and HD 208440 are to the left of the points in the figure in Browning et al., indicating fluxes consistent with the average interstellar value. On the other hand, the data for 9 Cep, HD 209339, and HD 217035A lie to the right, suggesting fluxes along these lines of sight are higher than the average interstellar value. An UV enhancement factor as large as 100 may be needed to explain our H_2 results. Because other processes leading to high-J level populations and because the presence of less shielded foreground gas that is mainly atomic were not considered, I_{uv} values inferred from H_2 data should be regarded as upper limits for the chemical analysis (§6.1). Furthermore, such large fluxes are usually associated with correspondingly high densities and temperatures in photon dominated regions (e.g., Knauth et al. 2001), but our CO data indicate subthermal excitation in diffuse molecular gas. Therefore, our use of the average interstellar radiation field ($I_{uv} \sim 1$) seems reasonable under these circumstances along lines of sight with CN absorption. In other words, it appears that the material studied here is sufficiently far from the background star (~ 3 pc) that only the average interstellar field is important.

For the 14 directions with H_2 measurements, knowledge of both the b-value for each component and the mean kinetic temperature along the line of sight yields an estimate for the turbulent velocity in each component. The turbulent velocity for all but one of the 72 components is ≈ 1 km s^{-1}. The results for gas toward Cep OB2 and OB3 are indistinguishable. Since the material along these sight lines is predominantly atomic, a comparison based on sound speeds derived from a ratio of specific heats of $5/3$ is appropriate. For temperatures of 70 to 80 K, the sound speed is also about 1 km s^{-1}. Thus, the turbulence appears to be sonic. One component toward λ Cep is the exception: its turbulent velocity is ~ 2.5 km s^{-1}. The component resembles the CH$^+$-like CH component toward ζ Oph (Lambert et al. 1990; Crawford 1997).

7. Discussion

7.1. Distribution of Species

In previous sections, similarities in average b-values and correlations between column densities allowed us to suggest that some species coexist, while others probe different portions of a diffuse molecular cloud with typical visual extinctions of 1 to 2 mag. We here investigate the distribution of observed species from other aspects. If two species coexist, their spectral profiles along a given line of sight should appear similar, although their line strengths may be quite different. For easy comparison, we construct apparent optical depth (AOD) profiles (Savage & Sembach 1991) for the absorption lines, and overplot scaled AOD profiles for different species on a given line of sight. Figure 4 shows the comparison of these profiles along the line of sight toward HD 207308. The scaling factors differ from species to species and from panel to panel. For instance, CH and K I AOD profiles are scaled by factors of 1/2.84 and 1/15.1 in the middle panel, respectively.

By comparing AOD profiles for six species on each of our sight lines, we find, along a given sight line, (1) that the CN profile is the narrowest one, whereas the Ca II profile is the widest one, (2) that CH and K I profiles are usually similar in both width and shape, and (3) that in most cases, CH^+ and Ca I profiles are wider than CH, in roughly 80% of the cases for CH^+, and 60% for Ca I. The similarity among the profiles for the three species is not all that clear. In some cases, Ca I profiles are similar to CH^+ ones. In other cases, they may be more similar to those of CH than to those of CH^+. It may depend upon the local gas density. Here we are assuming line width, or equivalently b-value, is a measure of the distribution along the line of sight.

The comparison of AOD profiles suggests that Ca II is the most widely distributed among the six species, followed by CH^+ and Ca I, then K I and CH, and finally CN. Distributions of velocity components reinforces this statement. Figure 5 is a histogram plot for distributions of velocity components with respect to V_{LSR} along lines of sight in Cep OB2 (excluding components toward HD 206267A and λ Cep because component structures are not available for some species). The Figure shows that Ca II components are much more widely distributed than those of other species, and that distributions of CH, K I, and Ca I have very similar shape. This again indicates correlations among the latter three species.

Previous studies of diffuse molecular clouds (Federman et al. 1984) showed that the CN molecule is produced in observable quantities only after significant amounts of precursor molecules, such as CH and C_2, are available. In particular, the relationship between $N(CN)$ and $N(H_2)$ has a slope much steeper than that seen for $N(CH)$ vs. $N(H_2)$ (e.g., Federman 1982; Danks et al. 1984). Federman et al. (1984) attributed the steepness in slope to the

number of chemical steps before the molecule can be detected. Higher densities facilitate the transformation along the chemical sequence. Our observations reveal that CN has the narrowest profile, smallest b-values, and smallest number of velocity components among the species. In other words, CN is the least widely distributed and occupies the smallest volume among the species. Therefore, we believe that CN mainly resides only in denser regions of diffuse molecular clouds, and that no observable amount of CN is present in low density clouds or in cloud envelopes. The correspondence between CO and CN noted above suggests, for the most part, that the same applies to CO. This is consistent with the slope found for $N(\text{CO})$ vs. $N(\text{H}_2)$ — see § 7.4; CO can exist in regions with somewhat lower densities because faster (ion-molecule) reactions dominate its production (e.g., van Dishoeck & Black 1986).

In §§ 4 and 5, we showed that there are two kinds of CH-containing material: CN-like CH, which is associated with CN production, and CH^+-like CH, which is related to the formation of CH^+. This suggests that CH could coexist with either CN and CH^+. Since in all velocity components where CN is detected, CH is observed, we believe that CH exists in the whole volume where CN resides. On the other hand, generally wider profiles, more components, and larger b-values indicate that CH occupies a larger volume than does CN.

Similarities in b-values, AOD profiles, and a good correlation between their column densities all suggest that CH and K I generally coexist, or share a large fraction of their volumes in diffuse clouds. The combined set of facts leads us to believe that these two species can also exist in less dense gas, or less dense regions of clouds (such as envelopes) where CN is not present. A relevant question is to what extent do the CH and K I distributions extend into the region of lower density. In other words, what is the lowest gas density that can be probed by CH and K I observations? The relatively low ionization potential (4.341 eV) for K I suggests that it cannot exist in a very low density environment because it must be shielded from photoionization. In addition, the b-values of CH and K I are only slightly larger than that of CN. This indicates that their distributions cannot extend much beyond the region containing CN. Therefore, CH and K I appear to be distributed in high- and moderately high-density regions of diffuse clouds ($n \geq 30$ cm^{-3}). We also note that K may be depleted onto grains in very high density gas, and that there are some K I components without corresponding CH components. The facts suggest that K I may be absent in extremely dense regions of clouds, but slightly extend to less dense regions compared to CH (also see § 5.3).

Because the AOD profiles for CH^+ and Ca I are generally wider than those for CH and K I, these species may occupy bigger volumes of a cloud. On the other hand, similar b-values and strong correlations between $N(\text{K I})$ and $N(\text{Ca I})$ suggest that K I and Ca I share a large

fraction of their volumes. According to the chemical models of Federman (1982) and Danks et al. (1984) and the depletion characteristics of calcium (see next section), both CH^+ and Ca I cannot have a significant abundance in dense gas where CN and CH reside. CH^+ and Ca I only exist in less dense gas, and so their distributions extend throughout the envelope of a cloud beyond those of CH and K I. This is also consistent with the fact that Ca I has a greater first ionization potential than does K I (6.1 eV vs. 4.3 eV). On the other hand, neither CH^+ nor Ca I can exist in a very low density enviroment where insignificant amounts of H_2 (e.g., Federman 1982) are available for CH^+ production and where the main forms of Ca will be Ca II or Ca III. Thus, we conclude that CH^+ and Ca I mainly exist in moderately high- to intermediate-density gas ($n \sim 10$–300 cm^{-3}).

The Ca II ion is the most widely distributed species among the species we observed. Its absorption can arise in components not seen in neutral atoms or molecules (see Figs. 4 and 5), and its b-value is the largest among our observed species. Considering that Ca readily depletes onto grains, Ca II should exist in a moderately high to low-density enviroment. Figure 6 is a schematic showing the distributions of species we discussed. In some low density clouds, the density is so low that molecules are not present even in the densest regions. Ca II may be the only species among those studied here in such clouds.

7.2. Ca and K Depletions

Cardelli, Federman & Smith (1991) noticed that the Ca I absorption line profiles were more similar to those of CH^+ than to those of CH on some lines of sight and suggested that calcium depletion depends on the density. For total column density along a line of sight, they found an inverse linear relationship between the ratios $N(CN)/N(CH)$ and $N(Ca\ I)/N(CH)$. Using a simple model, assuming photoionization equilibrium in predominantly neutral gas, where carbon is the primary source of electrons and where the space densities and column densities have the same functional form, they concluded that the fractional density of calcium varies roughly as n^{-3}, due to the depletion. However, Welty et al. (2003) recently found a steeper relationship between the column density ratios with a slope of $\lesssim -2.5$, implying that the density dependence of Ca column density is not steeper than $n^{-1.8}$.

Comparing our spectra, we found some cases where the Ca I profiles are similar to those of CH^+ and in other cases the similarity is with CH profiles. A closer examination shows that the similarities may depend on the local gas density where the absorption arises. In most (roughly 75%) of the high density cases [relatively large ratio of $W_\lambda(CN)/W_\lambda(CH)$ or strong CN absorption], Ca I profiles resemble those of CH^+. For intermediate density clouds [small ratio of $W_\lambda(CN)/W_\lambda(CH)$ or no CN detection], we did not find a clear trend, but we

note that in some cases, the Ca I, CH$^+$, and CH profiles are quite similar. These findings on profiles are consistent with the picture for the distribution of species drawn in § 7.1. In a high n enviroment, a large fraction of CH absorbers come from a region where no detectable amount of Ca I and CH$^+$ reside, whereas along the line of sight a large fraction of Ca I and CH$^+$ absorbers originate from a common volume. Then, Ca I profiles are more similar to those of CH$^+$ than those of CH. For a intermediate density cloud, the three species may coexist over a large fraction of the volume, and their profiles would be similar. Therefore, qualitatively, the calcium depletion depends upon the local gas density.

As already noted, using total column densities, Cardelli et al. (1991) and Welty et al. (2003) obtained different slopes for the relationship between $N(CN)/N(CH)$ and $N(Ca\ I)/N(CH)$. Figure 7 presents relations between the ratios $N(CN)/N(CH)$ and both $N(Ca\ I)/N(CH)$ and $N(K\ I)/N(CH)$ for individual components. Fair correlations are found between the ratios with correlation coefficients of -0.68 and -0.40 and corresponding correlation confidences of 99.98% and 99.50%, respectively. Regression fits yield slopes of -1.03 ± 0.15 and -2.03 ± 0.20 for the respective relationships. Within the framework of Cardelli et al., these slopes imply that the calcium and potassium column densities are proportional to $n^{-2.9}$ and $n^{-2.0}$, respectively, due to their depletions. However, caution should be exercised in applying the framework because assumptions may not be valid. These species do not occupy exactly the same volume in a cloud, as stated in § 7.1, and Welty et al. (2003) argued that the photoionization equilibrium may not strictly hold in diffuse clouds. While the inferred density dependence due to depletion may not be very accurate, it appears that calcium depletion varies more steeply on local density than potassium does, as suggested by both this analysis and by the slope in Figure 3.

7.3. Cloud Structure

7.3.1. Large-scale Structure

The Cepheus bubble, at a distance of ≈ 750 pc from the Sun, has been the subject of many investigations. Radio H I and CO observations revealed that the bubble has structures on a scale of a few pc. Expanding shells of dense gas around H II regions have been inferred in previous studies of CO emission from the molecular clouds around OB stars. The large-scale CO molecular cloud shows a clumpy and irregular structure, with small cloudlets having sizes of a few parsecs (e.g., Patel et al. 1995, 1998; Weikard et al. 1996). Figure 8 is the map of CO emission for the Cep OB2 region adapted from Patel et al. (1995; 1998), with our stars projected onto the map. According to their locations on the CO map, we divided our stars into several groups (that do not reflect coeval stellar groups). For example, we

consider HD 206267A, C, D, and HD 206773 as one group. They are associated with the same CO cloud, cloud number 18 in Table 2 of Patel et al. (1998). HD 207538, HD 208266, and ν Cep are in another group associated with cloud number 21. The AOD profiles for absorption lines are very similar for a given species in a group. The lines of sight in each group have most velocity components in common, especially within the V_{LSR} range in which CO emission was detected from a cloudlet. Spectra for sight lines passing near edges of CO clouds show strong CN absorption. However, there are some exceptions. For example, the line of sight toward 14 Cep passes near the edge of one CO cloud, but only one weak CN component with $N(CN) = 0.45 \times 10^{12}$ cm^{-2} was detected. There is no nearby CO cloud toward HD 207198, but strong CN and CO absorption was detected on the line of sight. Since 14 Cep has the smallest extinction [$E(B-V)$=0.35] and the smallest estimated distance (650 pc) among our lines of sight in Cep OB2, 14 Cep most likely is located in front of its nearby CO cloudlet. In general, our data are consistent with the large-scale structure suggested by maps of CO radio emission. The V_{LSR} of CN , CO, and CH components on a line of sight (including those toward ρ Oph and Cep OB3) are in a range within which CO emission is detected from a cloudlet. For IC 1396 in Cep OB2, this correspondence is consistent with the conclusion of Weikard et al. (1996) that much of the material seen in CO emission is in front of HD 206267. The sensitivity of absorption measurements at visible and UV wavelengths allows us to detect smaller molecular columns than is possible through emission line maps, providing further detail of cloud dispersal in regions of star formation.

7.3.2. Small-scale Structure

While it is well established that the column densities of some atomic (H I, Na I, K I) and molecular (H$_2$CO, OH) species vary on scales of 10 to 10^5 AU along diffuse sight lines, detailed information on the physical conditions causing the variations is generally not available. A key question posed by the observations is whether the subparsec structure is caused by density variations (e.g., Frail et al. 1994; Lauroesch & Meyer 1999; Crawford et al. 2000), by fluctuations in ionization equilibrium (Lauroesch & Meyer 1999; Welty & Fitzpartrick 2001), by the geometric structure of clouds (Heiles 1997), or by something else. A crucial point is to determine accurate physical conditions for the gas showing variations in column density. With gas densities inferred from a chemical model for CH, C$_2$, and CN (see § 6.1) for velocity components on lines of sight toward members of multiple star systems, we now discuss small scale structure in diffuse molecular gas.

There are three multiple star systems, ρ Oph A/B/C/D, HD 206267 A/C/D, and HD 217035 A/B, in our data set. Separations between members of systems range from 450 to

38,320 AU (0.02 to 0.18 pc). Substantial variations in CN absorption are observed among sight lines of ρ Oph. There are striking differences in the CN, CH, CH$^+$, Ca I, and K I profiles among the three sight lines of HD 206267. No CN is detected toward either line of sight in the HD 217035 system, but a significant difference in the CH$^+$ profiles for the two members of the system is observed. The corresponding column densities differ by a factor of $\sim$2 in individual velocity components.

Pan et al. (2001) discussed gas density variations on sight lines of the multiple star systems HD 206267 and HD 217035. Because Paper I employed a different method to determine column densities of individual components and a slightly different data reduction procedure, velocity component structures and their column densities might be slightly different from those in Pan et al. However, the conclusion of Pan et al. that the component gas densities can differ by factors of 5 between adjacent lines of sight is not altered. From Table 7, we see that the derived gas densities of the components toward members of HD 206267 at the same or similar V_{LSR} differ by factors of 2—7. (If the upper limits for gas density are considered, the difference can be as high as 10.) In the case of the ρ Oph multiple star system, the diffuse molecular cloud toward ρ Oph C has a density about twice that inferred along the other three nearby sight lines. While less dramatic than the results for the system HD 206267, the result for ρ Oph reinforces the conclusions of Pan et al. Density contrasts up to factors of 10 over scale lengths of 10,000 to 20,000 AU *are present* in the densest portions of diffuse clouds, those sampled by CN absorption; variations of the order of 10^4 suggested by 21 cm observations (e.g., Frail et al. 1994) must have a different origin. Possibilities include fluctuations in ionization equilibrium (Lauroesch & Meyer 1999; Welty & Fitzpatrick 2001) and the geometric structure of clouds (Heiles 1997). The smallest scale length probed by our measurements, 450 AU between ρ Oph A and B, shows no variation in modeled density greater than about 35%.

Cloud thicknesses for individual components (cloudlets) along the line of sight toward the background star can be estimated as well. The total column density of protons, N_{tot}(H), for a component can be estimated from our measurements of N(K I) (from Paper I) and the relationship between N(K I) and N_{tot}(H), $\log[N(\text{K I})] = (-26.9 \pm 2.7) + (1.8 \pm 0.1)$ $\log[N_{tot}(\text{H})]$ derived by Welty & Hobbs (2001), under the assumption that it applies to components although they used total column densities. Then n and N_{tot}(H) are used to estimate the thickness of a cloudlet. For the multiple star systems, ρ Oph and HD 206267, the thickness is within 50% of 1 pc, except for the two low-density components toward HD 206267A where the thickness is about 5 pc. Since n refers to the dense region where CN resides, the mean n for the whole cloudlet should be lower. Our estimates should then be regarded as lower limits. If the lower limits are not far below their true values, they suggest that some of the cloudlets (in Cep OB2) are sheet-like with aspect ratios of 5 to 10 because

maps of CO millimeter-wave emission show that a typical size of a cloudlet on the sky is a few parsecs (Patel et al. 1995, 1998; Weikard et al. 1996). Our results, therefore, provide evidence for the need to consider non-spherical geometries (Heiles 1997) when analyzing small scale structure in diffuse clouds.

7.4. Individual Cloud Systems

The diffuse gas associated with the three star-forming regions, Cep OB2, Cep OB3, and ρ Oph (belonging to Sco OB2), were observed. Table 8 lists the average number, $\langle M \rangle$, of velocity components per sight line for each species and the average column density of each component for each species.[6] The table shows that lines of sight toward Cep OB2 and Cep OB3 have many more Ca II and K I components than those toward ρ Oph. This is consistent with radio observations (Sargent 1977; Weikard et al. 1996; Patel et al. 1998), which revealed that clouds in Cep OB2 and Cep OB3 have complicated structures. Table 8 also reveals that Cep OB3 has the greatest mean number of Ca II and CH^+ components per sight line, the largest average column density per Ca II component, but the smallest corresponding values for CN among the three star-forming regions. This indicates that a larger fraction of low density material is probed by the lines of sight toward Cep OB3. Because CN resides only in the denser region of diffuse molecular clouds, while Ca II is widely distributed, the ratio, $\langle M_{CN} \rangle \times \langle N(CN) \rangle / (\langle M_{CaII} \rangle \times \langle N(Ca\ II) \rangle)$, may reflect the fraction of denser material in the clouds. The ratio for ρ Oph is about 2 and 10 times larger than for Cep OB2 and Cep OB3, respectively.

Lines of sight toward Cep OB3 have larger mean extinction, $E(B - V)$, (0.78 vs. 0.53 mag), greater $\langle M_{CaII} \rangle$, and larger $\langle N(Ca\ II) \rangle$ compared to those toward Cep OB2. This suggests that more material is intercepted along lines of sight in Cep OB3. However, Cep OB3 clouds have a lower mean density. This indicates that Cep OB2 clouds are geometrically thinner, along the line of sight, than Cep OB3 clouds.

Using total H_2 column densities from *Copernicus* observations, Federman (1982) and Federman et al. (1980) found that total CH and CO column densities along lines of sight

---

[6]CO column densities for individual components were obtained along 15 lines of sight toward Cep OB2 and Cep OB3 by analyzing *HST* and *FUSE* spectra — see § 3. Because different spectral resolutions comprise this sample, it may be not fully appropriate to include the CO results in the comparison. Still, our analyses show that CO has fewer components than CH but more than CN, and that, on average, sight lines toward Cep OB2 and Cep OB3 have about the same number of CO components per line of sight, but components in Cep OB2 have much larger mean column density.

were well correlated with total H_2 column densities. In the present study, we obtained total H_2 column densities along 15 sight lines toward Cep OB2 and Cep OB3 based on $FUSE$ observations. Although $FUSE$ provides higher quality spectra, we still could not extract reliable column densities for individual components due to very large line optical depths, thus preventing us from seeking correlations between N(CH) and N(CO) with N(H_2) on a component basis as we did for other relationships in § 5. Figure 9 shows plots of total column density for CH and CO versus H_2 along the 15 lines of sight. In general, the Figure reveals the same trends, as previous studies (Federman et al. 1980; Federman 1982; Danks et al. 1984): N(CH) and N(CO) increase with increasing N(H_2) with a slope of 0.95 ± 0.10 for CH (Cep OB2) and 3.16 ± 0.34 (Cep OB2) and 2.93 ± 0.58 (Cep OB3) for CO. For comparison, Danks et al. (1984) obtained a slope of 0.90 ± 0.10 for N(CH) vs. N(H_2), and Federman et al. (1980) found a slope of about 2 for the CO trend. However, Cep OB2 sight lines are clearly distinguished from those toward Cep OB3. Lines of sight toward Cep OB2 have higher N(CH) and N(CO) column densities for a given N(H_2). This implies that the physical conditions in these star-forming regions, such as average gas density, may be quite different. Since there are a larger fraction of CN components toward stars in Cep OB2, the diffuse molecular clouds toward Cep OB2 have higher average gas density. The direction toward HD 217312 in Cep OB3 represents an intermediate case: there is a large enough fraction of CN components to place it among the CH data for Cep OB2, but not enough for the CO data because CO traces the densest gas with CN.

Absorption from the diffuse molecular gas for a specific star-formation region shows similar overall structure, and the length scales probed by our measurements are similar for the three star-forming regions. However, the diffuse molecular clouds associated with Cep OB3 exhibit different characteristics compared to those associated with ρ Oph and Cep OB2. The cloudlets have lower gas density and lower total molecular mass (see § 2). Compared with Cep OB2 and Cep OB3, material in the ρ Oph star-forming cloud is much more compact. This is consistent with our finding that lines of sight toward Cep OB2 and Cep OB3 have many more Ca II and K I components. It is not clear, however, if the differences seen in the diffuse gas surrounding the parent molecular clouds are related to the star formation histories in the clouds. The molecular cloud system associated with Cep OB3 is currently forming its second generation of stars, whereas a third generation of stars is forming in clouds associated with Cep OB2 and possibly in the ρ Oph region. The older stellar subgroup in Cep OB3 has an age of $\sim$ 7 Myr, whereas the oldest stars in Cep OB2 and in Sco OB2 (to which ρ Oph belongs) are about 15 Myr, with the second older groups $\sim$ 7 Myr (see § 2). It would be useful to clarify possible connections between physical conditions and differences in star-forming history. It seems that star formation in Cep OB2 and Cep OB3 has proceeded via sequential triggering (Patel et al. 1995; Sargent 1979), whereas star formation scenarios for

ρ Oph are still a matter of debate (de Geus 1989; Sartori et al. 2003). de Geus et al. (1989) derived respective ages of 11–12, 14–15, and 5–6 Myr for three stellar subgroups, LCC, UCL, and US, of Sco OB2. They argued that either the classic picture of sequential star formation (Blaauw 1964; Elmegreen & Lada 1977) is not valid for the Sco OB2 Association as a whole because the oldest subgroup, UCL, is in between the two younger ones, or for some unknown reason massive star formation was initiated near the middle of the original giant molecular cloud. However, Pan (2002) found that uncertainties in the above derived ages are large, and that LCC and UCL might actually have a similar age and thus star formation in Sco OB2 may not contradict the model for sequential star formation. Based on spatial positions and ages of stellar subgroups in Sco OB2, Pan (2002) conjected that LCC and UCL could represent the first generation stars, the members of US the second, and the newly formed stars in the ρ Oph cloud the third generation. If all three star-forming regions follow the classical picture of sequential star formation (Elmegreen & Lada 1977), and assuming stellar generations in Sco OB2 as that suggested by Pan (2002), then the age periods between the 1st and 2nd and between the 2nd and 3rd are about 7–9 and 5–6 Myr in all three star-forming regions. Support for this picture comes from Sartori et al. (2003). They found that the US subgroup is 4–8 Myr old and that LCC and UCL have the same age, 16–20 Myr, by adopting Hipparcos distances, newer isochrones, and temperatures derived from the spectral types. However, from the spatial distribution, the space velocity, and the age distribution of stars in Sco OB2, Sartori et al (2003) argued that star formation in ρ Oph, most likely, is connected to star formation in nearby spiral arms rather than sequential triggering. This may explain why material in ρ Oph is more compact than in Cep OB2 and Cep OB2.

8.   Summary

We obtained and analyzed FUV data on H_2 and CO along 15 lines of sight toward Cep OB2 and Cep OB3 to complement the optical survey results of Paper I. Average b-values of individual components are found to be consistent with those obtained from ultra-high resolution spectra. The b-values for CN components are also consistent with those derived from the doublet ratio method (Strömgren 1948; Gredel et al. 1991). The inferred CN excitation temperatures range from 2.55 to 2.89 K, with an average of 2.75 $\pm$ 0.10 K, indicating that no significant excitation in addition to that due to the CMB is present in the diffuse molecular clouds in our sample.

With our large high-resolution data set, we examined some possible correlations between column densities of different species based on individual velocity components. In general, relationships are found to be tighter compared with those based on total column densities.

The main correlations are the following. (1) There are two kinds of CH in diffuse molecular gas: CN-like CH and CH^+-like CH. Disentangling the amount of CH in each appears possible when utilizing the relation between column densities of CH^+-like CH and of CH^+. (2) Column densities of CN and CH components are well correlated. The relationship becomes even stronger if the corresponding column density of CH^+-like CH is subtracted from the total CH column. A close correspondence between CN and CO is also seen. (3) The trends between CH and K I, and Ca I and K I show tight correlatations. The slope of the relationship for $N(\text{Ca I})$ vs. $N(\text{K I})$ is 0.60 ± 0.04, significantly smaller than 1.0, which may suggest that calcium depletion depends more strongly on local density than does potassium depletion.

We investigated the spatial distributions of species by analyzing apparent optical depth profiles, distributions of components with respect to V_{LSR}, b-values, ionization potentials of elements, and correlations between column densities. These analyses show that different species are restricted to specific density regions. The CN and CO molecules mainly reside in denser regions of diffuse molecular clouds. No observable amount of CN is present in low density clouds or in cloud envelopes. The species CH and K I are distributed in high- and moderately high-density gas ($n \geq 30 \text{ cm}^{-3}$). (K I may not be present in very dense regions of clouds because there may be enhanced K depletion.) CH^+ and Ca I are mainly distributed in moderately high- and intermediate-density regions ($n \sim 10\text{--}300 \text{ cm}^{-3}$). The Ca II ion is the most widely distributed among the observed species; it can exist in moderately high-density regions but favors a relatively low density environment.

Several correlations and analyses show that both Ca and K may be depleted onto grains in denser gas, and that the Ca depletion has a steeper dependence on local density. Within the framework of Cardelli et al (1991), our data suggest that Ca column density varies roughly as $n^{-2.9}$, whereas K column is proportional to $n^{-2.0}$ due to their depletions. However, we note that their assumptions involving space densities and column densities may not be applicable.

Gas densities for individual velocity components where CN is detected were inferred from a chemical model. The inferred gas densities are independent of assumptions about cloud shape, on which some previous calculations relied. Based on these derived gas densities, we examined the large- and small-scale structure of clouds. In general, our data are consistent with the large-scale structure suggested by maps of CO radio emission. Our analysis reveals the presence of variations in gas density among sight lines in two multiple star systems, ρ Oph and HD 206267. The gas density is seen to vary by factors of 5—10 over scales of $\sim 10,000$ AU. This indicates that observed column density variations are due in part to a change in gas density. However, variations of the order of 10^4 suggested by 21 cm observations (e.g., Frail et al. 1994) must have a different origin. Cloud thicknesses for individual components (cloudlets) are estimated to be ~ 1pc, which may suggest that some of the cloudlets are

sheet-like with aspect ratios of 5 to 10. The estimation of cloud thickness provides evidence for the need to consider non-spherical geometries (Heiles 1997) when analyzing small-scale structure in diffuse clouds.

Comparisons show that there are both similarities and differences in general character-istics of diffuse gas in the three star-forming regions, ρ Oph, Cep OB2 and Cep OB3. For example, cloud turbulence in the three regions does not differ significantly (but note that Cep OB3 seems to have consistently larger b-values than ρ Oph and Cep OB2). Clouds in Cep OB2 and Cep OB3 have more complex (clumpy) structures than those in ρ Oph; in other words, material in ρ Oph is more compact than in Cep OB2 and Cep OB2. The molecular cloudlets associated with Cep OB3 have lower gas density and lower total molecular mass, compared to those associated with ρ Oph and Cep OB2. The differences may be related to the star formation histories for the regions.

This paper presents analyses of the physical and chemical structure of the diffuse gas in star-forming regions based on absorption at visible and UV wavelengths. As in Federman et al. (1997) and Knauth et al. (2001), such analyses provide results for foreground diffuse molecular gas that are both consistent and complement results of the denser gas probed at longer wavelength. The combined set of data yields a comprehensive view of the effects of star formation on molecular clouds.

REFERENCES

Abraham, P., Balazs, & Kun M. 2000, A&A, 354, 645

Aiello, S., Barsella, B., & Chlewicki, G. et al. 1988, A&AS, 73, 195

Andersson, B-G, Wannier, P. G., & Crawford, I. A. 2002, MNRAS, 334, 327

André, M. K., Oliveira, C. M., Howk, J. C. et al. 2003, ApJ, 591, 1000

Assousa, G. E., Herbst, W., & Turner, K. K. 1977, ApJ, 218, L13

Bevington, P. R., & Robinson, D. K. 1992, *Data Reduction and error Analysis for the Physical Sciences*, Boston, WCB McGraw-Hill

Blaauw, A. 1958, AJ, 63, 186

Blaauw, A. 1964, ARA&A, 2, 213

Cardelli, J. A., Federman, S. R., & Smith, V. V. 1991, ApJ, 381, L17

Cardelli, J. A., Suntzeff, N. B., Edgar, R. J., & Savage, B. D. 1990, ApJ, 362, 551

Cartledge, S. I. B., Lauroesch, J. T., Meyer, D. M., & Sofia, U. J. 2004, ApJ, 613, 1037

Cartledge, S. I. B., Meyer, D. M., Lauroesch, J. T., & Sofia, U. J. 2001, ApJ, 562, 394

Chaffee, F. H., & White R. E. 1982, ApJS, 50, 169

Chan, W. F., Cooper, G., & Brion, C. E. 1993, Chem. Phys., 170, 123

Clark, P. C., Bonnell, I. A., Zinnecker, H., & Bate, M. R. 2005, MNRAS, in press.

Cox, P. L., & Smith, B. W. 1974, ApJ, 189, L105

Crane, P., Lambert, D. L., & Sheffer, Y. 1995, ApJS, 99, 107

Crawford, I. A., 1995, MNRAS, 277, 458

Crawford, I. A., 1997, MNRAS, 290, 41

Crawford, I.A., Howarth, I.D., Ryder, S.D., & Stathakis, R.A. 2000, MNRAS, 319, L1

Crenny, T., & Federman, S.R. 2004, ApJ, 605, 278

de Geus, E. J. 1992, A&A, 262, 258

de Geus, E. J., Bronfman, L., & Thaddeus, P., 1990, A&A, 231, 137

de Geus, E. J., de Zeeuw, P. T., & Lub, J. 1989, A&A, 216, 44

de Zeeuw, P. T., Brown, A. G. A., de Bruijne, J. H, J., et al. 1999, AJ, 117, 354

Doppmann, G. M., Jaffe, D. T., & White, R. J. 2003, ApJ, 126, 3043

Danks, A. C., Federman, S. R., & Lambert, D. L. 1984, A&A, 130, 62

Danks, A. C., & Lambert, D. L. 1983, A&A, 124, 188

Draine, B. T. 1978, ApJS, 36, 595

Draine, B. T., & Katz, N. 1986, ApJ, 306, 655

Elmegreen, B. G., & Lada, C. J. 1977, ApJ, 214, 725

Eidelsberg, M., Jolly, A., Lemaire, J. L., Tchang-Brillet, W.-ÜL., Breton, J., & Rostas, F. 1999, A&A, 346, 705

Federman, S. R. 1982, ApJ, 257, 125

Federman, S. R., Danks, A. C., & Lambert, D. L. 1984, ApJ, 287, 219

Federman, S. R., Fritts, M., Cheng, S., Menningen, K. M., Knauth, D. C., & Fulk, K. 2001, ApJS, 134, 133

Federman, S. R., Glassgold, A. E., Jenkins, E. B., & Shaya, E. J., 1980, ApJ, 242, 545

Federman, S. R., & Huntress, W. T. Jr. 1989, ApJ, 338, 140

Federman, S. R., Knauth, D. C., Lambert, D. L., & Andersson, B-G, 1997, ApJ, 489, 758

Federman, S. R., Lambert, D. L. 1988, ApJ, 328, 777

Federman, S. R., Strom, C. J., Lambert, D. L., Cardelli, J. A., Smith, V. V., & Joseph, C. L. 1994, ApJ, 424, 772

Federman, S. R., Welty, D. E., & Cardelli, J. A. 1998, ApJ, 481, 795

Fitzpatrick, E. L. & Massa, D. 1990, ApJS, 72, 163

Frail, D. A., Weisberg, J. M., Cordes, J. M., & Mathers, C., 1994, ApJ, 436, 144

Garmany, C. D. 1973, AJ, 78, 185

Garrison, R. F. 1970, AJ, 75, 1001

Garrison, R. F., & Kormendy, J. 1976, PASP, 88, 865

Gredel, R., van Dishoeck, E. F., & Black, J. H. 1991, A&A, 251, 625

Green, T. P., & Young, E. T. 1992, ApJ, 395, 516

Gry, C., Neheme, C., Le Bourlot, J., Boulanger, F. & Pineau des Forets, G. 2005, in *Astrophysics in the Far Ultraviolet*, ASP Conf. Ser., eds. Sonneborn, Moos & Andersson

Heiles, C. 1997, ApJ, 481 193

Hobbs, L. M. 1976, ApJ, 203, 143

Isobe, T., & Feigelson, E.D. 1990, BAAS, 22, 917

Isobe, T., Feigelson, E.D., & Nelson, P.I. 1986, ApJ, 306, 490

La Valley, M., Isobe, T., & Feigelson, E.D. 1992, BAAS, 24, 839

Lupton R., 1993, *Statistics in Theory and Practice*, Princeton Univ. Press, Princeton

Jenkins, E. B., & Meloy, D. A., 1974, ApJ, 193, L121

Jenkins, E. B., & Tripp, T. M. 2001, 137, 297

Knauth, D. C., Federman, S. R., Pan, K., Yan, M., & Lambert, D. L., 2001, ApJS, 135, 201

Kun M., Balazs, L. G., & Toth, I. 1987, Ap&SS, 134, 211

Lambert D. L., & Danks, A. C. 1986, ApJ, 340, 314

Lambert D. L., Sheffer, Y., & Crane, P. 1990, ApJ, 359, L19

Laoroesch, J. L., & Meyer, D. M. 1999, ApJ, 519, L181

Loren, R. B. 1989, ApJ, 338, 902

Marri, S.& White, S. D. M. 2004, MNRAS, 345, 561

Massa, D., Savage, B. D., & Fitzpatrick, E. L. 1983, ApJ, 266, 662

McKee, C. F. 1990, in Evolution of the Interstellar Medium, ed. L. Blitz (San Francisco: ASP), 3

McKee, C. F. & Tan, J. C. 2003, ApJ, 585, 850

Megier, A., Krelowski, J., Patriarchi, P., & Aiello, S. 1997, MNRAS, 292, 853

Moreno-Corral, M.A., Chavarria, K.C., De Lara, E., & Wagner, S. 1993, A&A, 273, 619

Morton, D. C., & Noreau, L. 1994, ApJS, 5, 301

Pan, K., 2002, PhD Thesis (University of Toledo)

Pan, K., Federman, S. R., Cunha, K., Smith, V. V., & Welty, D. E. 2004, ApJS, 151, 313 (Paper I).

Pan, K., Federman, S. R., & Welty, D. E. 2001, ApJ, 558, L105

Patel N. A., Goldsmith P. F., Heyer M. H., Snell, R. L., & Pratap, R., 1998, ApJ, 507, 241

Patel, N. A., Goldsmith P. F., Snell, R. L., & Xie, T. 1995, ApJ, 447, 721

Phelps, R. & Barsony, M. 2004, AJ, 127, 420

Rachford, B. L., Snow, T. P., Tumlinson, J. et al. 2002, ApJ, 577, 221

Sargent, A. I. 1977, ApJ, 218, 736

Sargent, A. I. 1979, ApJ, 233, 163

Sartori, M. J., Lepine, J. R. D., & Dias, W. S., 2003, A&A, 404, 913

Savage, B.D., Bohlin, R.C., Drake, J.F., & Budich, W. 1977, ApJ, 216, 291

Savage, B. D., Massa, D., Meade, M., & Wesselius, P. R. 1985, ApJS, 59, 397

Savage, B. D. & Sembach, K. R. 1991, ApJ, 379, 245

Sheffer, Y., Federman, S. R., & Andersson, B.-G. 2003, ApJ, 597, L29

Strömgren, B. 1948, ApJ, 108, 244

Thornton, K., Gaudlitz, M., Janka, H.-Th., & Steinmetz, M. 1998, ApJ, 500, 95

van Dishoeck, E. F. & Black, J. H., 1986, ApJS, 62, 109

Welty, D.E., & Fitzpatrick, E.L. 2001, ApJ, 551, L75

Welty, D. E., & Hobbs, L. M. 2001, ApJS, 133, 345

Welty, D. E., Hobbs, L. M.,& Morton, D. C. 2003, ApJS, 147, 61

Welty, D. E., Morton, D. C., & Hobbs, L. M. 1996, ApJS, 106, 533

Weikard, H., Wouterloot, J. G. A., Castets, A., Winnewisser, G., & Sugitani, K. 1996, A&A, 309, 581

Yu, Z., Nagahama, T., & Fukui, Y. 1996, ApJ, 471, 867

Zsargó, J. & Federman, S. R 2003, ApJ, 589, 319

Table 1.   FUV Data Summary

Star	Satellite	Spectra	S/N	Molecule
Cep OB2				
HD203374A	*FUSE*	B03001	50	H_2
	HST	O5LH08	25	CO
HD206165/9 Cep	*FUSE*	B03002	25	H_2, CO
HD206267A	*HST*	O5LH09	30	CO
HD206773	*FUSE*	B07109	70	H_2, CO
	HST	O5C04T	25	CO
HD207198	*HST*	O59S06	25	CO
HD207308	*FUSE*	B03003	20	H_2
	HST	O63Y02	60	CO
HD207538	*HST*	O63Y01	55	CO
HD208266	*HST*	O63Y03	60	CO
HD208440	*FUSE*	B03004	75	H_2
	HST	O5C06M	25	CO
HD209339	*FUSE*	B03005	70	H_2
	HST	O5LH0B	35	CO
HD210839/λ Cep	*HST*	O54304	45	CO
Cep OB3				
HD216532	*FUSE*	A05102	15	H_2, CO
HD216898	*FUSE*	A05103	20	H_2, CO
HD217035A	*FUSE*	A05104	25	H_2, CO
HD217312	*FUSE*	P19305	35	H_2, CO

Table 2.   Molecular Results[a]

Target	$N(\mathrm{H_2})$ $(10^{20}\ \mathrm{cm^{-2}})$	$T_{1,0}$ (K)	$N(\mathrm{CH})$ $(10^{13}\ \mathrm{cm^{-2}})$	$N(\mathrm{CO})$ $(10^{15}\ \mathrm{cm^{-2}})$	$\mathrm{CH/H_2}$ (10^{-8})	$\mathrm{CO/H_2}$ (10^{-6})
			Cep OB2			
HD203374A	5.04(0.08)	76(1)	2.22(0.2)	2.56(0.11)	4.40(0.45)	5.08(0.23)
9 Cep	5.98(0.26)	68(4)	2.04(0.2)	1.53(0.04)	3.41(0.37)	2.56(0.13)
HD206267A	7.24(0.63)	65(5)	3.03(0.3)	10.1(0.7)	4.19(0.56)	14.0(1.6)
HD206773	2.93(0.05)	94(1)	1.12(0.1)	0.23(0.03)	3.82(0.39)	0.80(0.09)
HD207198	6.76(0.59)	66(5)	3.53(0.4)	2.65(0.12)	5.22(0.69)	3.92(0.39)
HD207308	7.28(0.17)	57(1)	3.21(0.3)	8.60(0.95)	4.41(0.45)	11.8(1.3)
HD207538	8.13(1.05)	73(8)	3.81(0.4)	2.49(0.25)	4.69(0.77)	3.06(0.50)
HD208266	7.4–10[b]	$\cdots$	3.35(0.3)	11.2(1.2)	$\cdots$	$\cdots$
HD208440	2.21(0.03)	75(2)	1.16(0.1)	0.16(0.01)	5.25(0.53)	0.72(0.03)
HD209339	1.79(0.03)	90(1)	0.79(0.1)	0.09(0.01)	4.41(0.45)	0.49(0.06)
λ Cep	6.92(0.61)	72(6)	2.08(0.2)	2.47(0.20)	3.01(0.40)	3.57(0.43)
			Cep OB3			
HD216532	12.7(0.4)	83(8)	2.02(0.2)	1.42(0.11)	1.59(0.17)	1.12(0.09)
HD216898	11.1(0.3)	86(6)	2.85(0.3)	1.09(0.08)	2.12(0.22)	0.98(0.08)
HD217035A	9.00(0.25)	75(1)	1.68(0.2)	0.37(0.03)	1.87(0.19)	0.41(0.03)
HD217312	6.38(0.16)	76(3)	2.56(0.3)	0.24(0.03)	4.01(0.41)	0.38(0.05)

[a]Uncertainties are denoted within parentheses.

[b]$N(\mathrm{H_2})$ is predicted from $N(\mathrm{CH})$ and $N(\mathrm{CO})$.

Table 3.   Column Densities for $\mathrm{H_2}$ Rotational Levels[a]

Target	$\mathrm{Log}_{10}(N_J)$							
	Total	$J=0$	$J=1$	$J=2$	$J=3$	$J=4$	$J=5$	$J=6$
				Cep OB2				
HD203374A	20.70(0.01)	20.41(0.01)	20.39(0.02)	18.59(0.12)	18.17(0.06)	15.91(0.04)	14.95(0.14)	13.94(0.12)
9 Cep	20.78(0.02)	20.53(0.01)	20.40(0.06)	18.74(0.08)	18.21(0.15)	17.64(0.20)	15.80(0.41)	14.97(0.05)
HD207308	20.86(0.01)	20.70(0.01)	20.35(0.03)	18.70(0.10)	17.86(0.12)	17.14(0.14)	16.00(0.37)	14.15(0.12)
HD208440	20.34(0.01)	20.05(0.01)	20.02(0.02)	18.42(0.02)	18.13(0.11)	16.04(0.17)	15.02(0.11)	14.18(0.16)
HD209339	20.25(0.01)	19.87(0.01)	20.00(0.01)	18.36(0.05)	18.02(0.07)	17.41(0.05)	16.40(0.07)	14.06(0.04)
				Cep OB3				
HD216532	21.10(0.02)	20.76(0.04)	20.83(0.06)	19.27(0.05)	17.93(0.31)	17.52(0.30)	17.03(0.12)	14.59(0.18)
HD216898	21.05(0.02)	20.69(0.02)	20.78(0.04)	19.08(0.07)	18.31(0.08)	17.19(0.20)	15.37(0.15)	14.37(0.09)
HD217035A	20.95(0.02)	20.66(0.01)	20.63(0.02)	18.98(0.08)	18.34(0.23)	17.91(0.27)	15.97(0.19)	14.49(0.19)

[a]Uncertainties are denoted within parentheses.

Table 4.   Average b-values (in km s^{-1}) for Individual Components

Species	Star-forming Region			Overall	
	Cep OB2	Cep OB3	ρ Oph	b	# of components
CN	0.83±0.11	0.84±0.11	0.80±0.05	0.83±0.11	50
CO	0.59±0.20	0.77±0.35	$\cdots$	0.66±0.28	53
CH	1.04±0.17	1.10±0.19	0.91±0.11	1.04±0.18	125
CN-like CH	0.90±0.11	$\ldots$	$\ldots$	0.90±0.11	12
CH$^+$-like CH	1.10±0.15	1.12±0.18	0.96±0.14	1.10±0.16	78
CH$^+$	1.96±0.23	1.97±0.23	1.80±0.23	1.96±0.23	111
Ca I	0.94±0.16	1.07±0.13	1.03±0.11	0.96±0.16	119
K I	0.88±0.21	1.08±0.22	0.87±0.16	0.92±0.22	224
Ca II	1.61±0.26	1.75±0.19	1.35±0.40	1.62±0.28	350

Table 5. Molecular Correlations for Cloud Components toward Cep OB2

Target	Species	Cloud Component Structure							RMS[a]	$\frac{\mathrm{RMS(CH)}}{\mathrm{RMS(CN)}}$
HD203374A	CO	.01	.00	.50	.14	.34	.00	.01	···	···
	CN	···	···	.46	.18	.36	···	···	0.0233	···
	CH	.05	.04	.32	.20	.28	.06	.05	0.0828	3.6
HD206267A	CO	.07	.83	.07	.02	.00	.01		···	···
	CN	.03	.81	.10	.06	···	···		0.0277	···
	CH	.14	.29	.07	.29	.07	.14		0.2553	9.2
HD206773	CO	.18	.72	.10					···	···
	CN	···	1.00	···					0.2007	···
	CH	.14	.40	.46					0.2790	1.4
HD207198	CO	.22	.09	.47	.16	.02	.04		···	···
	CN	.28	···	.52	.20	···	···		0.0545	···
	CH	.15	.08	.29	.28	.08	.12		0.1015	1.9
HD207308	CO	.12	.00	.84	.04				···	···
	CN	···	···	.82	.18				0.0927	···
	CH	.07	.09	.57	.27				0.1847	2.0
HD207538	CO	.01	.05	.33	.59	.02	.00		···	···
	CN	···	.12	.31	.38	.19	···		0.1143	···
	CH	.06	.18	.31	.31	.11	.03		0.1337	1.2
HD208266	CO	.00	.87	.12	.00	.01			···	···
	CN	···	.77	.16	.07	···			0.0576	···
	CH	.01	.39	.37	.12	.11			0.2520	4.4
λ Cep	CO	.72	.28						···	···
	CN	.74	.26						0.0200	···
	CH	.62	.38						0.1000	5.0

[a]Of the CO structure *vs.* the CN or CH structure. Undetected CN components (···) were assigned the value ".00" for rms calculations. CO components designated by ".00" were modeled to be $\leq$ .005.

Table 6. Relationships among Column Densities Involving Individual Components

Y	X	N	r	p	$\log[N(Y)] = A + B \times \log[N(X)]$		
					A	B	d_{rms} [a]
CH	CH^+	90	0.37	0.0004	5.65±1.30	0.55±0.11	0.288
CH^+-like CH [b]	CH^+	36	0.77	0.0000	0.60±1.34	0.95±0.13	0.124
CN	CH	48	0.80	0.0000	−12.54±1.98	1.91±0.16	0.127
CN	CN-like CH	12	0.97	0.0000	−10.25± 1.72	1.74±0.13	0.053
CN	CH^+-cor CH	40	0.87	0.0000	−10.08±1.76	1.73±0.13	0.120
Ca I	Ca II	117	0.47	0.0000	−0.08±0.96	0.81±0.08	0.220
Ca I	K I	114	0.69	0.0000	2.88±0.47	0.60±0.04	0.171
K I	CH	123	0.87	0.0000	−0.85±0.55	0.96±0.04	0.134
K I	Ca II	223	0.55	0.0000	−10.94±0.72	1.89±0.06	0.277

[a]Root mean square distance of points from the fit line.

[b]Only components with $\log[N(CH^+)] \leq 12.6$ are fitted.

Table 7. Chemical Results

Cloud[a]	I_{uv}	τ_{uv}	T (K)	n (cm^{-3})	N_o(CH)	N_o(C$_2$)	N_p(C$_2$) (10^{12} cm^{-2})	N_o(CN)	N_p(CN)
					ρ Oph				
ρ Oph D	1	2.08	50	425	19.5	. . .	18.7	2.1	2.1
ρ Oph C	1	2.04	40	1100	19.2	. . .	44.4	6.0	6.0
ρ Oph A	1	2.04	50	625	14.9	26.0	21.4	2.1	2.6
ρ Oph B	1	2.04	50	450	16.8	. . .	18.0	2.0	2.0
					Cep OB2				
HD 203374A(-1.2)	1	3.69	50	90	6.9	. . .	8.5	1.0	0.9
HD 203374A($+1.2$)	1	3.69	50	60	4.5	. . .	3.8	0.4	0.4
HD 203374A($+3.1$)	1	3.69	50	80	6.3	. . .	7.0	0.8	0.8
HD 204827(-9.2)	1	6.66	50	30	7.0	. . .	4.0	1.3	1.3
HD 204827(-6.4)	1	6.66	50	30	5.3	. . .	3.1	0.9	1.0
HD 204827(-4.3)	1	6.66	30	200	31.4	. . .	45.3	17.1	17.5
HD 204827(-2.0)	1	6.66	30	110	13.6	. . .	16.6	5.8	5.8
HD 204827($+0.5$)	1	6.66	30	125	26.9	. . .	34.2	12.3	12.3
9 Cep(-1.3)	1	2.72	50	200[b]	5.0	3.5[c]	5.3	0.7	0.5
9 Cep($+0.3$)	1	2.72	50	300[b]	5.7	6.0[c]	8.7	1.2	0.9
9 Cep($+3.7$)	1	2.72	50	175[b]	4.1	2.5[c]	3.8	0.5	0.4
HD 206183	1	2.56	50	250	7.8	. . .	8.7	1.0	1.0
HD 206267A(-4.7)	1	3.13	50	80	4.1	2.6[c]	2.7	0.3	0.3
HD 206267A(-2.7)	1	3.13	50	1150[b]	8.8	61.1[c]	49.8	7.0	10.1
HD 206267A(-0.9)	1	3.13	50	525[b]	2.1	7.9[c]	7.1	0.9	1.1
HD 206267A($+0.9$)	1	3.13	50	60	9.0	4.4[c]	4.5	0.5	0.4
HD 206267C(-3.0)	1	2.82	50	725	9.8	. . .	33.4	4.9	4.9
HD 206267C(-0.8)	1	2.82	50	250	2.4	. . .	3.4	0.4	0.4
HD 206267C($+0.8$)	1	2.82	50	425	8.9	. . .	19.9	2.6	2.5
HD 206267D(-4.3)	1	2.26	50	400	8.0	. . .	10.4	1.2	1.2
HD 206267D(-0.8)	1	2.26	50	650	5.3	. . .	10.6	1.3	1.3
HD 206773	1	2.50	50	225	4.5	. . .	4.3	0.45	0.46
HD 207198(-6.2)	1	3.63	50	150	5.3	8.5[c]	9.8	1.3	1.1
HD 207198(-2.1)	1	3.63	50	150	10.1	15.6[c]	18.6	2.4	2.2
HD 207198(-0.2)	1	3.63	50	50	9.8	5.9[c]	6.6	0.9	0.7
ν Cep	1	2.10	50	300	5.1	. . .	4.4	0.45	0.46
HD 207308(-2.4)	1	3.00	50	600	18.4	. . .	62.3	9.0	9.1
HD 207308(-0.5)	1	3.00	50	300	8.6	. . .	16.7	2.0	2.0
HD 207538(-4.4)	1	3.92	50	60	7.0	. . .	5.0	0.6	0.6
HD 207538(-2.5)	1	3.92	50	90	11.7	. . .	12.0	1.5	1.5
HD 207538(-0.5)	1	3.92	50	110	11.8	. . .	14.5	1.8	1.8
HD 207538($+1.9$)	1	3.92	50	150	4.4	. . .	7.0	0.9	0.9
	5	3.92	50	700	4.4	. . .	6.6	0.9	0.9
	1	3.92	50	275	2.3[d]	. . .	5.8	0.9	0.9
HD 208266(-4.4)	1	3.10	50	375	13.0	. . .	33.0	4.4	4.4
HD 208266(-2.8)	1	3.10	50	90	12.4	. . .	8.9	0.9	0.9
HD 208266(-0.6)	1	3.10	50	125	4.0	. . .	3.9	0.4	0.4
13 Cep(-2.0)	1	4.48	50	325	17.4	. . .	34.0	7.5	7.7
13 Cep(-0.3)	1	4.48	50	125	9.1	. . .	9.5	1.7	1.7

Table 7—Continued

Cloud[a]	I_{uv}	τ_{uv}	T (K)	n (cm^{-3})	N_o(CH)	N_o(C$_2$)	N_p(C$_2$) (10^{12} cm^{-2})	N_o(CN)	N_p(CN)
13 Cep(+1.5)	1	4.48	50	150	19.4	. . .	23.1	4.5	4.3
14 Cep	1	1.37	50	725	4.2	. . .	4.2	0.45	0.45
λ Cep(−2.3)	1	2.36	50	425	12.9[e]	12.6[c]	19.4	2.6	2.1
λ Cep(−0.4)	1	2.36	50	225	7.9[e]	4.4[c]	6.6	0.9	0.7
Cep OB3									
HD 216532	1	2.50	65	550	11.2	. . .	23.3	3.1	3.0
HD 216898	1	3.59	65	100	5.4	. . .	6.6	0.8	0.8
HD 217312(+0.0)	1	2.86	65	350	1.6	. . .	3.1	0.4	0.4
HD 217312(+5.2)	1	2.86	65	175	4.2	. . .	4.4	0.5	0.5
HD 217312(+7.2)	1	2.86	65	110	8.1	. . .	5.5	0.6	0.6

[a]If more than one cloud containing CN appears along a line of sight, the velocity is given in parentheses.

[b]Average of results for C$_2$ and CN.

[c]Scaled line-of-sight N(C$_2$) to relative contributions from CN components.

[d]Column associated with CN-like CH only.

[e]N(CH) from Crane et al. 1995.

Table 8. Mean Number of Velocity Components per Sight Line and Average Column Density per Component

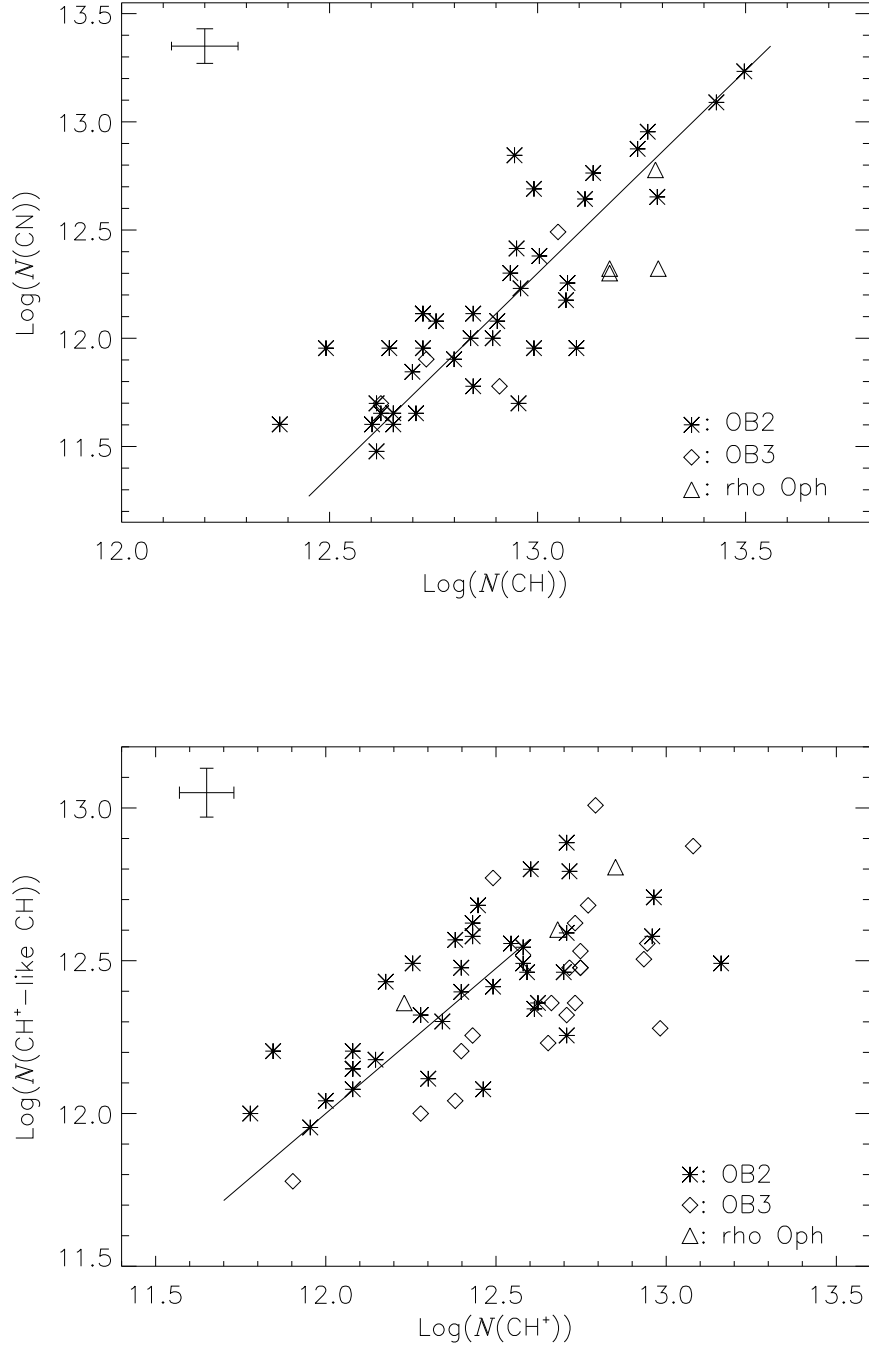| Species	$\langle$ M $\rangle$			$\langle N \rangle$ (cm^{-2})		
	Cep OB2	Cep OB3	ρ Oph	Cep OB2	Cep OB3	ρ Oph
Ca II	13.0	13.6	5.5	4.43×10^{11}	4.84×10^{11}	3.44×10^{11}
K I	8.0	9.8	4.0	2.12×10^{11}	1.52×10^{11}	2.51×10^{11}
Ca I	4.7	4.5	2.0	5.40×10^{9}	3.84×10^{9}	8.83×10^{9}
CH$^+$	3.9	6.6	2.0	3.56×10^{12}	5.24×10^{12}	5.58×10^{12}
CH	4.5	5.8	2.2	5.70×10^{12}	3.53×10^{12}	9.16×10^{12}
CN	2.0	1.0	1.0	2.60×10^{12}	1.08×10^{12}	3.05×10^{12}

Fig. 1.— Logarithmic plots of column densities. The error bars represent 20% uncertainties in N. *Top*: $N(CN)$ vs. $N(CH)$. The solid line presents our best fit

Bottom: $N(CH^+$-like CH) vs. $N(CH^+)$. The solid line is the best fit to components with $\log[N(CH^+)] \leq 12.6$ (see text for more detail). Here, and elsewhere, components toward Cep OB2 (asterisks), Cep OB3 (diamonds), and ρ Oph (triangles) are distinguished.
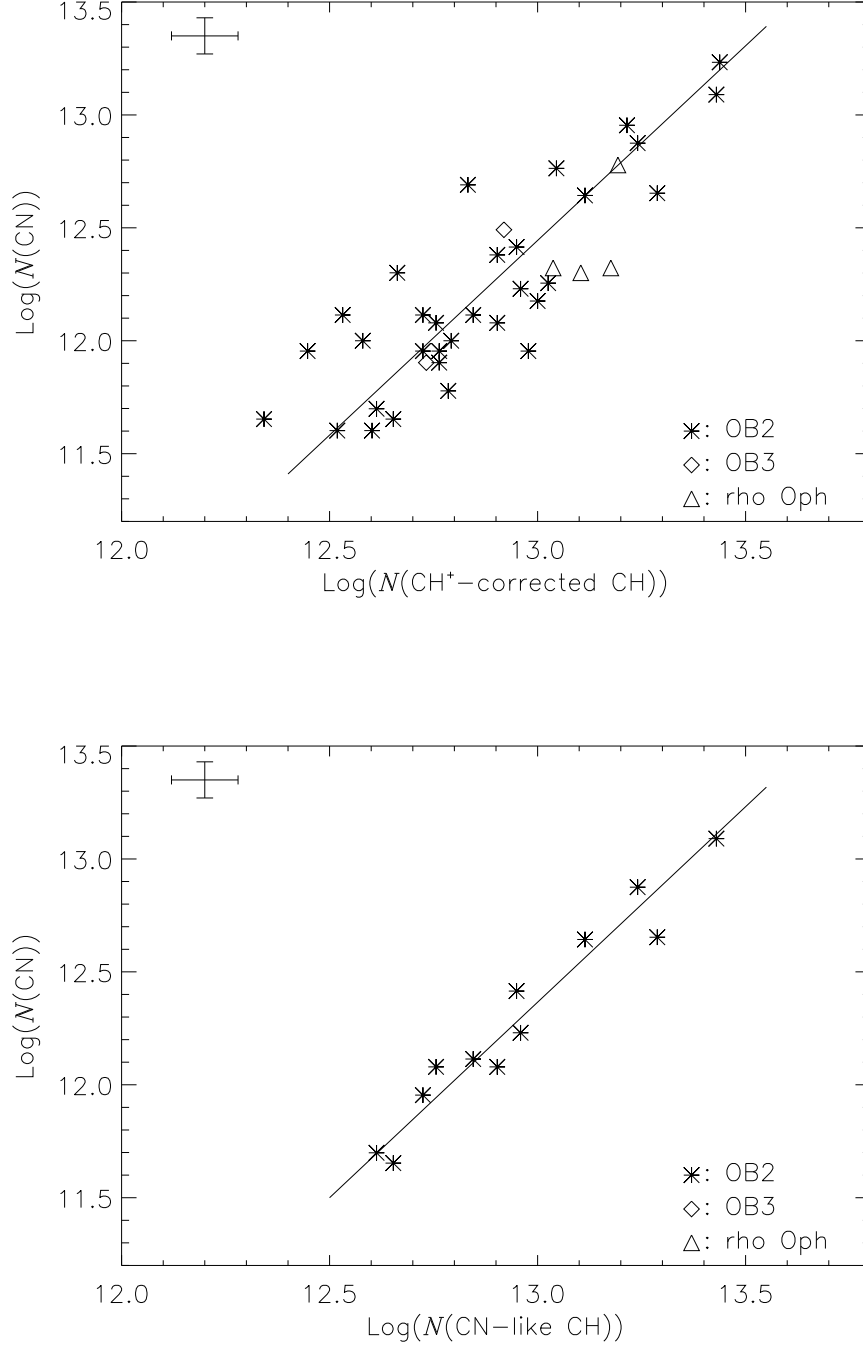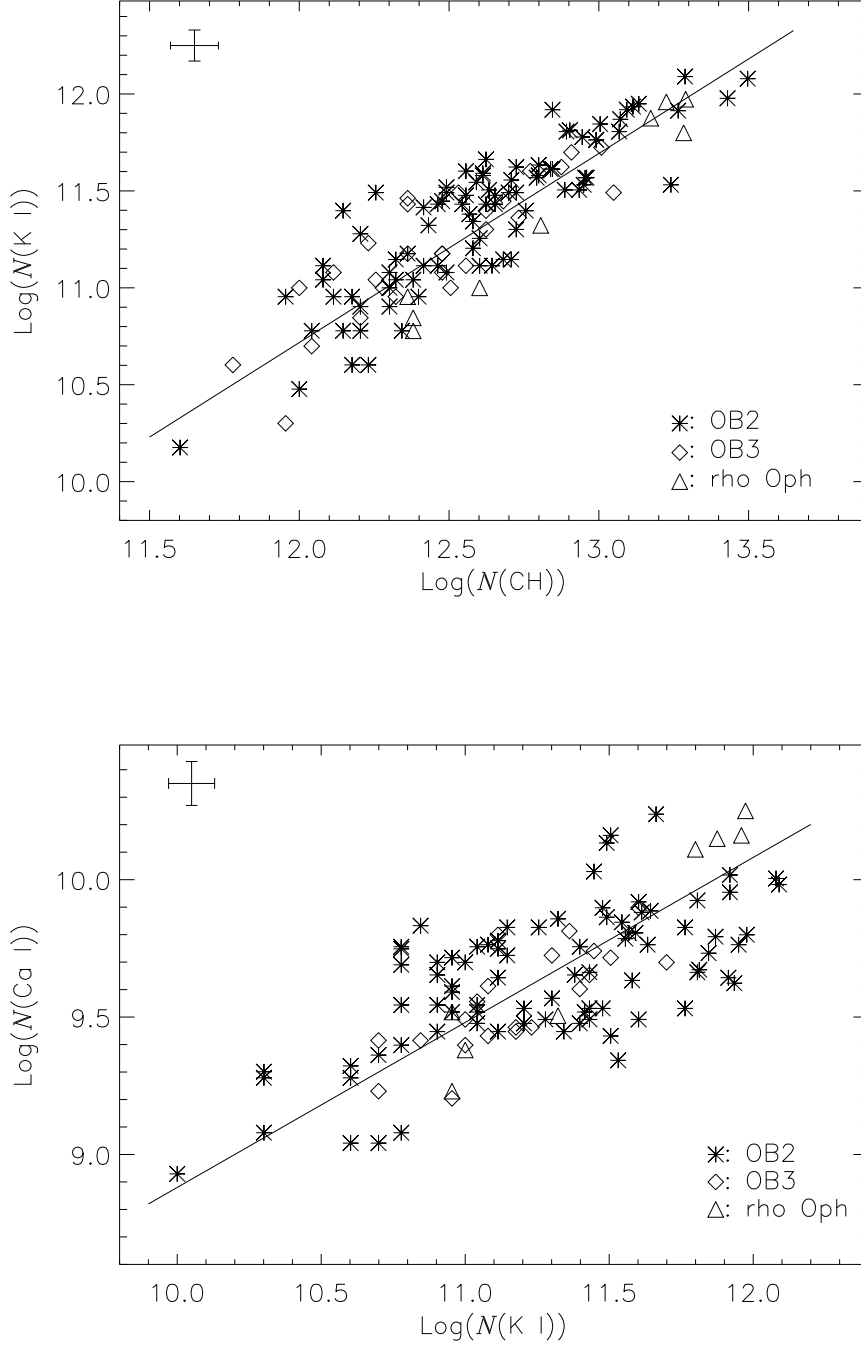
Fig. 2.— Logarithmic plots of column densities. The error bars represent 20% uncertainties in N. *Top*: $N(CN)$ vs. $N(CH^+$-corrected CH$)$. The solid line presents the best fit with a slope of 1.73, indistinguishable from the one between $N(CN)$ and $N(CN$-like CH$)$. *Bottom*: $N(CN)$ vs. $N(CN$-like CH$)$.

Fig. 3.— Logarithmic plots of column densities. The error bars represent 20% uncertainties in N. *Top*: $N(\text{K I})$ vs. $N(\text{CH})$. *Bottom*: $N(\text{Ca I})$ vs. $N(\text{K I})$. The solid line presents the best fit with a slope of 0.60 ± 0.04, which may suggest increasing calcium depletion in denser gas.
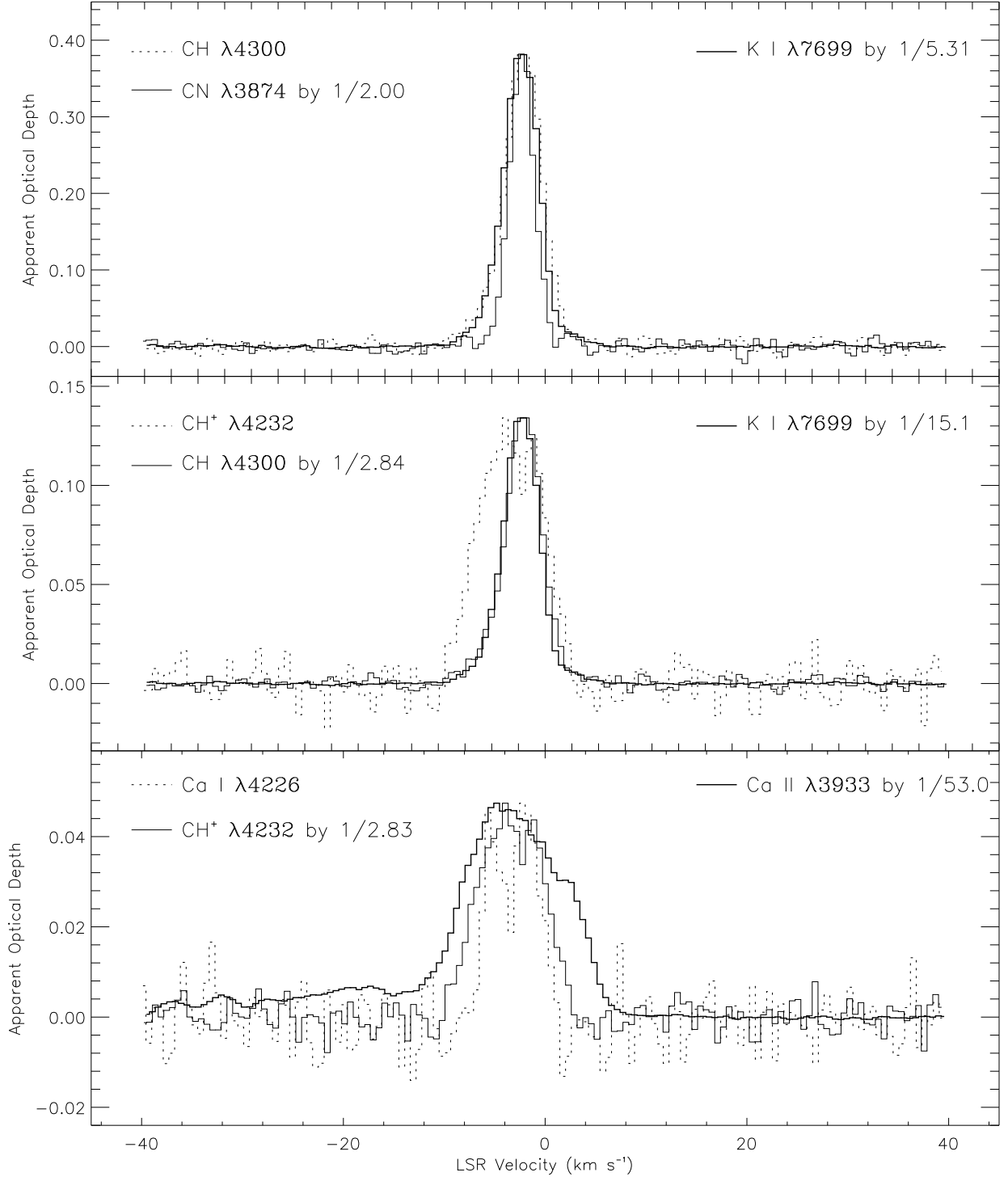
Fig. 4.— Plots of apparent optical depth profiles for different species on the line of sight toward HD 207308. Scaling factors are applied to individual profiles for easier comparison.
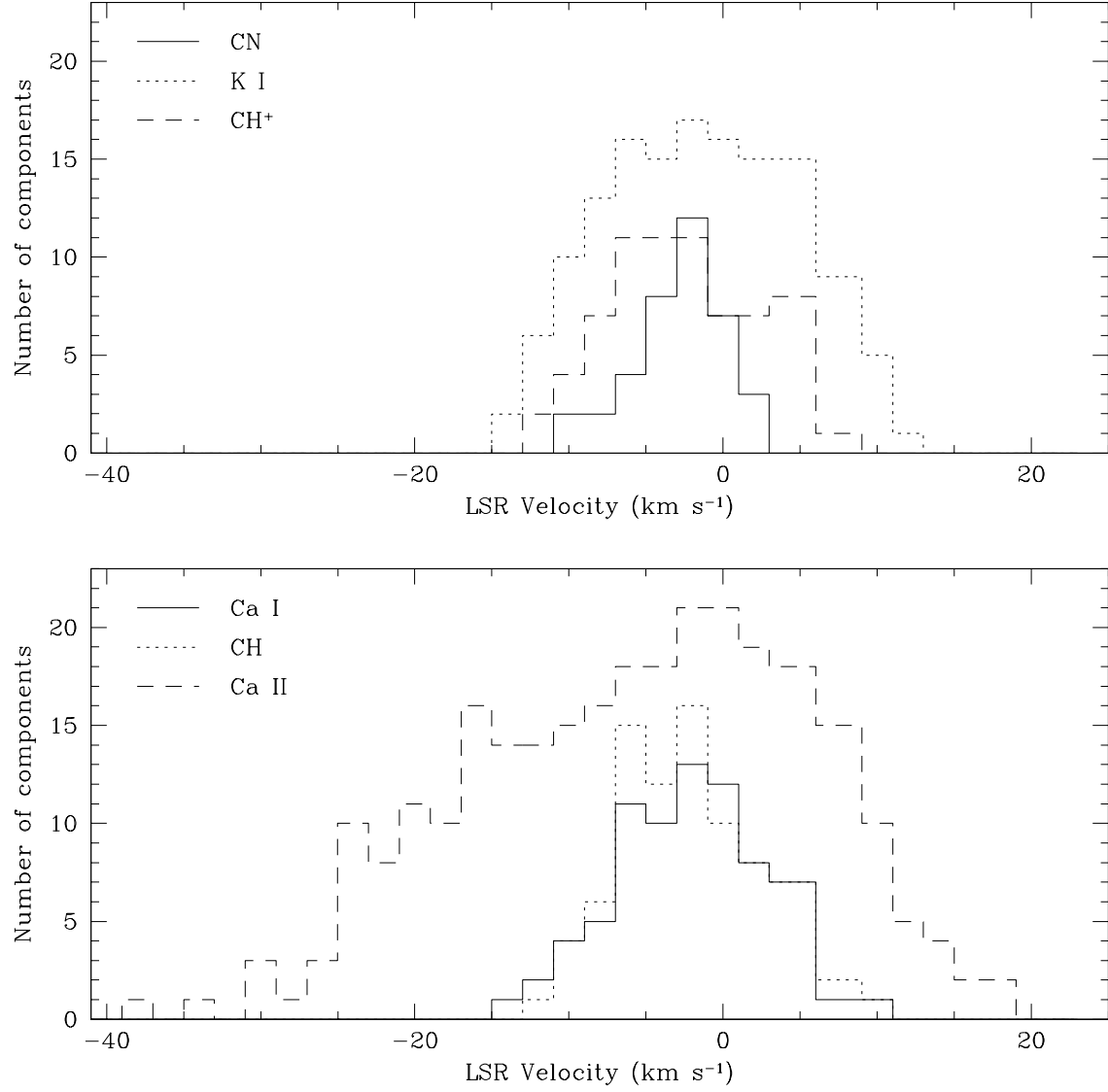
Fig. 5.— Distributions of velocity components along lines of sight toward Cep OB2 with respect to V_{LSR}.
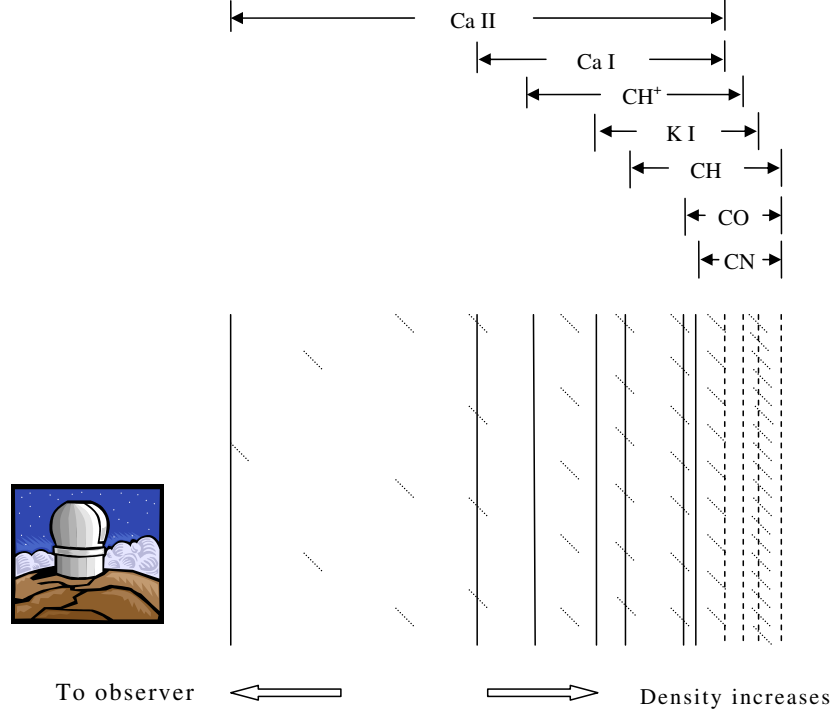
Fig. 6.— A schematic showing the inferred distributions of species in a diffuse cloud, here represented by a plane—parallel slab from the cloud surface to its denser regions. Different species are distributed according to gas density in the diffuse molecular gas (see text in §7.1). Dashed and solid vertical lines indicate the inner and outer boundaries of species distributions. In some low density clouds, CN and CH are not present. If the density is even lower, Ca II is the only one among these species present in the cloud. The spacing between hash-marks symbolizes (but not to scale) changes in gas density.
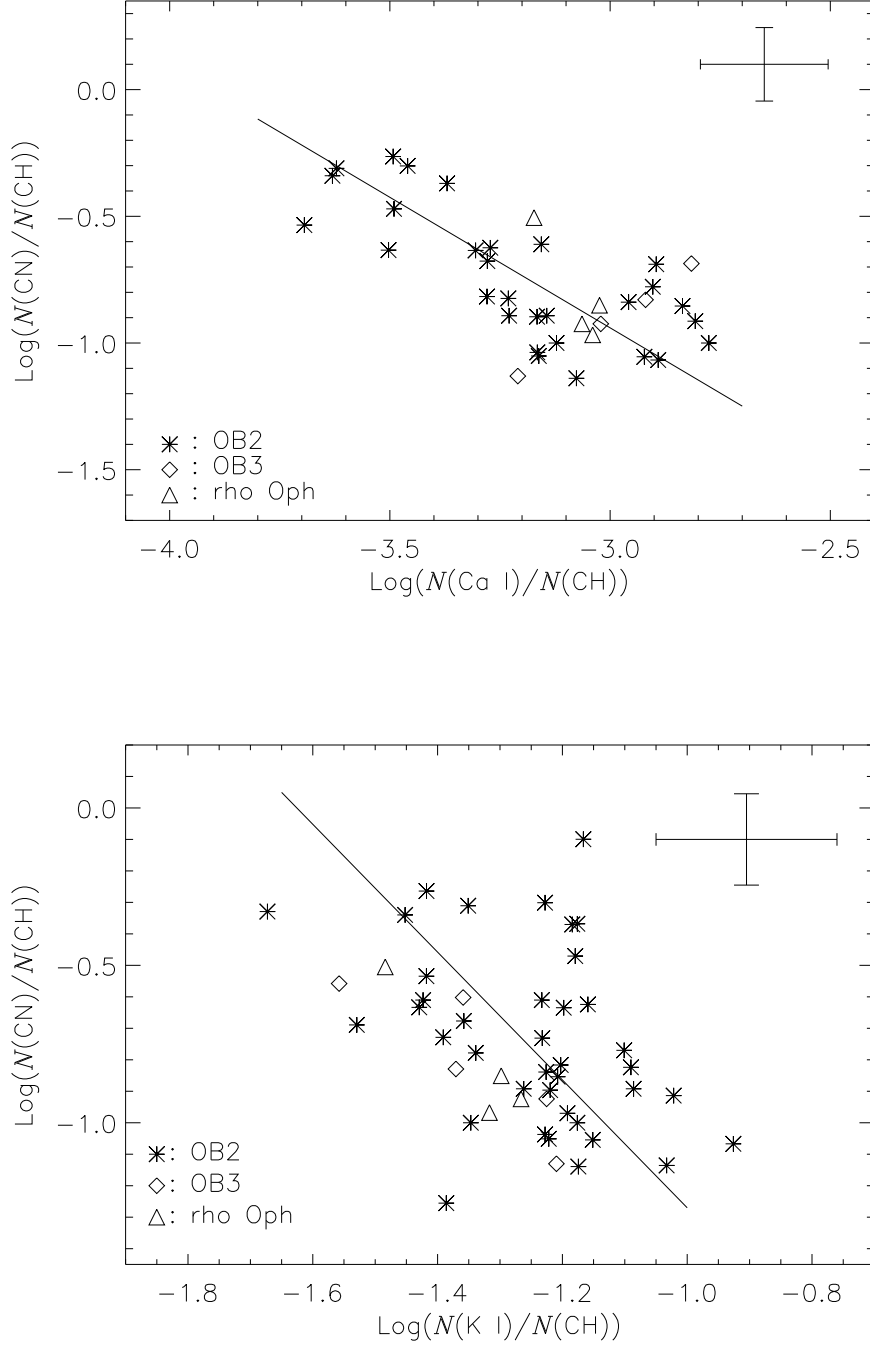
Fig. 7.— Logarithmic plots of column density ratios. The error bars represent 20% uncertainties in N. *Top*: $N(\mathrm{CN})/N(\mathrm{CH})$ vs. $N(\mathrm{Ca\ I})/N(\mathrm{CH})$. The solid line presents the best fit with a slope of -1.03 ± 0.15 *Bottom*: $N(\mathrm{CN})/N(\mathrm{CH})$ vs. $N(\mathrm{K\ I})/N(\mathrm{CH})$. The solid line presents the best fit with a slope of -2.03 ± 0.20.

500   400   300   200   100   0   -100

400

Cep OB2

300

200

HD208440
HD209339   HD207198

19 Cep   9 Cep
HD207308
HD208905   ν Cep
HD208266
HD207538
λ Cep   HD204827

14 Cep
HD206773
13 Cep   HD206183
HD206267A/B,C,D

HD203374A

100

0

-100

-200

Dec offset (arcmin)

Tr 37 - IC 1396

-50   HD204827

-100   B 161

HD206773

HD206267A/B, C, D

-150

HD206183

-200

Dec offset (arcmin)

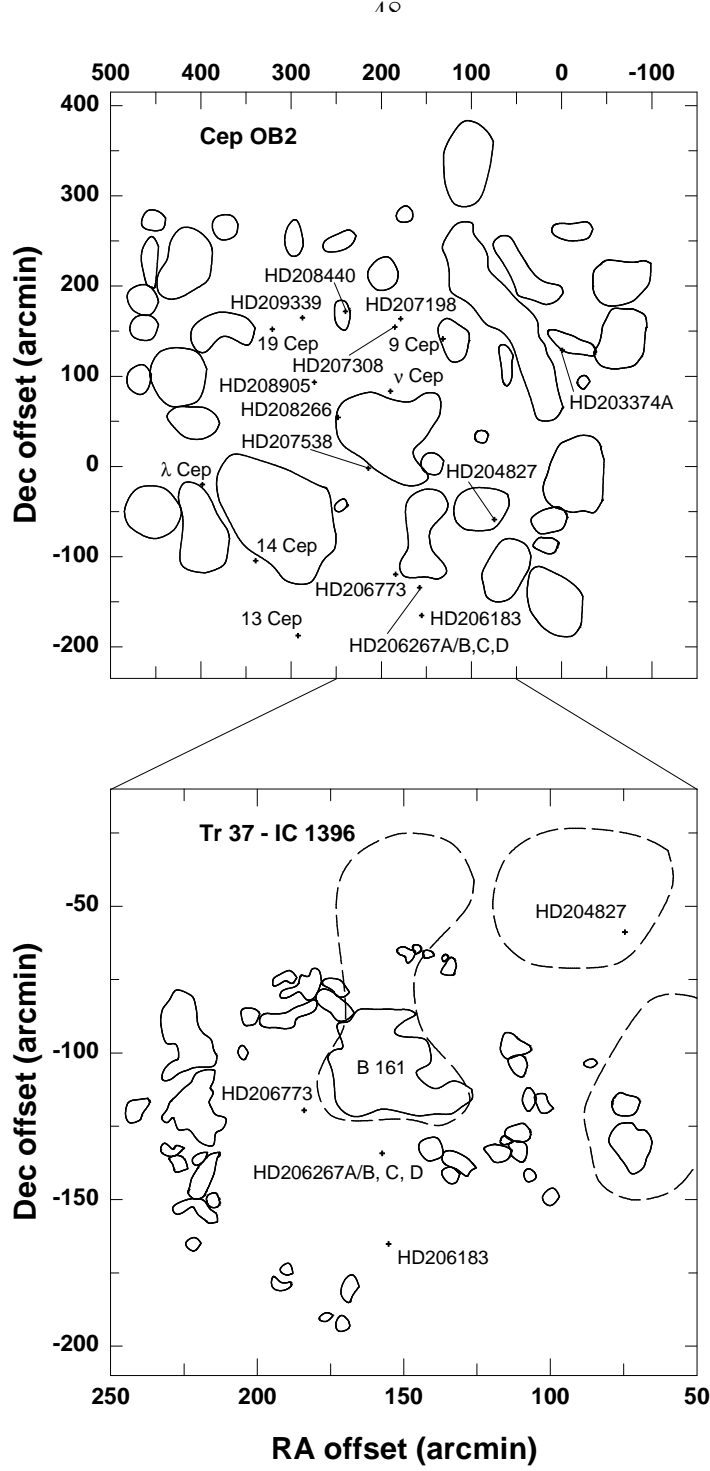250   200   150   100   50

RA offset (arcmin)

Fig. 8.— Map of CO emission across the Cep OB2 Association, adopted from Patel et al. (1995, 1998). Stars observed in the present study are projected onto the map. The lower panel is an expanded view of Tr 37/IC 1396. The dashed contours represent the entities in the upper panel.
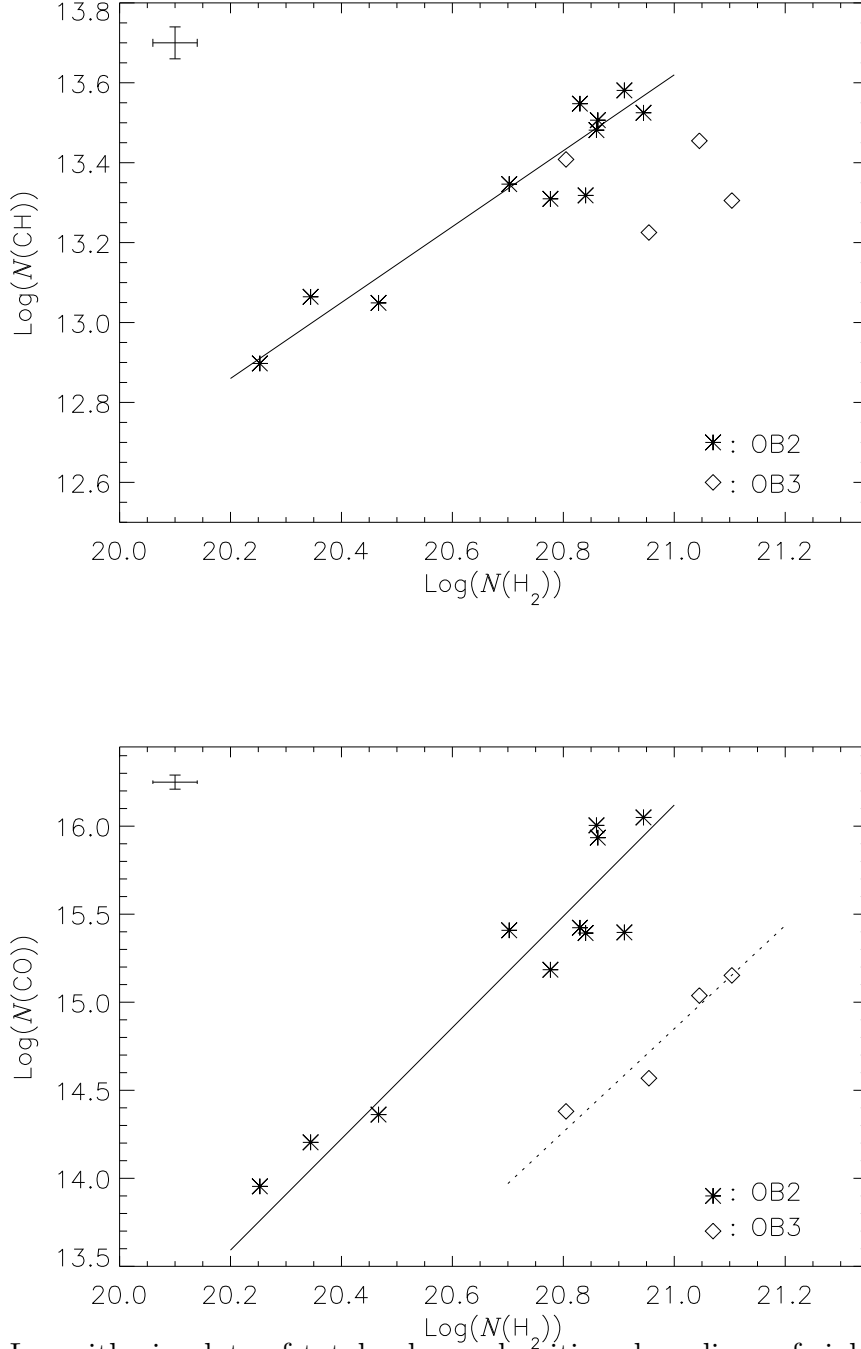
Fig. 9.— Logarithmic plots of total column densities along lines of sight in Cep OB2 and Cep OB3. The error bars represent 10% uncertainties in N. *Top*: $N(CH)$ vs. $N(H_2)$. The solid line shows the best fit to Cep OB2 data. *Bottom*: $N(CO)$ vs. $N(H_2)$. The solid line represents the best fit to Cep OB2 data, and the dashed one to Cep OB3 data. Note that, for a given $N(H_2)$, Cep OB2 sight lines have higher CH and CO column densities than lines of sight toward Cep OB3.